1 Aircraft-engine particulate matter emissions from conventional

2 and sustainable aviation fuel combustion: comparison of

3 measurement techniques for mass, number, and size

4 Joel C. Corbin[a], Tobias Schripp[b], Bruce E. Anderson[c], Greg J.

5 Smallwood[a], Patrick LeClercq[b], Ewan C. Crosbie[c,d], Steven Achterberg[e],

6 Philip D. Whitefield[e], Richard C. Miake-Lye[f], Zhenhong Yu[f], Andrew

7 Freedman[f], Max Trueblood[e], David Satterfield[e], Wenyan Liu[e], Patrick

8 Oßwald[b], Claire Robinson[c,d], Michael A. Shook[c], Richard H. Moore[c] and

9 Prem Lobo[a]

10 [a]Metrology Research Centre, National Research Council Canada, Ottawa, Ontario,

11 Canada

12 [b]German Aerospace Center (DLR), Institute of Combustion Technology, Stuttgart,

13 Germany

14 [c]NASA Langley Research Center, Hampton, Virginia, USA

15 [d]Science Systems and Applications, Inc., Hampton Virginia, USA

16 [e] Center of Excellence for Aerospace Particulate Emissions Reduction Research,

17 Missouri University of Science and Technology, Rolla, Missouri, USA

18 [f]Aerodyne Research, Inc., Billerica, Massachusetts, USA

19 Correspondence to: Joel C. Corbin (Joel.Corbin@nrc-cnrc.gc.ca) and Prem Lobo

20 (Prem.Lobo@nrc-cnrc.gc.ca)

Deleted: Department of Chemistry

22   0   AMT Feature: short summary (max. 500 characters incl. spaces)

23   The combustion of sustainable aviation fuels in aircraft engines produces

24   particulate matter (PM) emissions with different properties than conventional

25   fuels due to changes in fuel composition. Consequently, the response of various

26   diagnostic instruments to PM emissions may be impacted. We found no significant

27   instrument biases in terms of particle mass, number, and size measurements for

28   conventional and sustainable aviation fuel blends despite large differences in the

29   magnitude of emissions.

30   1   Abstract

31   Sustainable aviation fuels (SAFs) have different compositions compared to

32   conventional petroleum jet fuels, particularly in terms of fuel sulphur and

33   hydrocarbon content. These differences may change the amount and

34   physicochemical properties of volatile and non-volatile particulate matter (nvPM)

35   emitted by aircraft engines. In this study, we evaluate whether comparable nvPM

36   measurement techniques respond similarly to nvPM produced by three blends of

37   SAFs compared to three conventional fuels. Multiple SAF blends and conventional

38   (Jet A-1) jet fuels were combusted in a V2527-A5 engine, while an additional

39   conventional fuel (JP-8) was combusted in a CFM56-2C1 engine.

40   We evaluated nvPM mass concentration measured by three real-time

41   measurement techniques: photoacoustic spectroscopy, laser-induced

42   incandescence, and the extinction-minus-scattering technique. Various commercial

43   instruments were tested including three LII 300s, one PAX, one MSS+, and two

44   CAPS PM$_{SSA}$s. Mass-based emission indices (EI$_m$) reported by these techniques

45   were similar, falling within 30% of their geometric mean for EI$_m$ above 100

46   mg/kg$_{fuel}$ (approximately 10 µg PM m^{-3} at the instrument), this geometric mean

47   was therefore used as a reference value. Additionally, two integrative

48   measurement techniques were evaluated: filter photometry and particle size

49   distribution (PSD) integration. The commercial instruments used were one TAP,

50   one PSAP, and two SMPSs. These techniques are used in specific applications, such

51   as on-board research aircraft to determine PM emissions at cruise. EI$_m$ reported by

52   the alternative techniques fell within approximately 50 % of the mean aerosol-

Deleted: sampling

54 phase EI_m.

55 In addition, we measured PM-number-based emission indices using PSDs and

56 condensation particle counters. The commercial instruments used included TSI

57 SMPSs, a Cambustion DMS500, and an AVL APC, and the data also fell within

58 approximately 50 % of their geometric mean. The number-based emission indices

59 were highly sensitive to the accuracy of the sampling-line penetration functions

60 applied as corrections. In contrast, the EI_m data were less sensitive to those

61 corrections since a smaller volume fraction fell within the size range where

62 corrections were substantial. A separate, dedicated experiment also showed that

63 the operating laser fluence used in the LII 300 laser-induced incandescence

64 instrument for aircraft engine nvPM measurement is adequate for a range of SAF

65 blends investigated in this study. Overall, we conclude that all tested instruments

66 are suitable for the measurement of nvPM emissions from the combustion of SAF

67 blends in aircraft engines.

68   Keywords: non-volatile particulate matter, aircraft, emissions, sustainable

69   aviation fuels, black carbon

2   Introduction

71 Aircraft engine particulate matter (PM) emissions are composed of non-volatile

72 (black carbon, metal ash, oxygenated functional groups) and volatile components

73 (volatile organic compounds, nitrates, sulphates) (Gagné et al., 2021; Masiol and

74 Harrison, 2014; Petzold et al., 2011). The non-volatile particulate matter (nvPM)

75 emissions are formed in the combustor, while volatile particulate matter (vPM)

76 emissions, present in the gas phase at the engine exit, condense after emission.

77 Aircraft engines emit vPM with similar or greater orders of magnitude as nvPM,

78 especially after the vapour pressure of volatile species is lowered by oxidative

79 aging (Kiliç et al., 2018) or by cooling (Beyersdorf et al., 2014). The nvPM and vPM

80 are constituents of total PM which affects air quality, health, and climate. The

81 International Civil Aviation Organization (ICAO) has developed standards and

82 recommended practices (SARPs) for measuring the mass- and number-based

83 emissions of nvPM emitted from aircraft engines with maximum rated thrust >26.7

84 kN (ICAO, 2017). Currently, SARPs have not been established for vPM or total PM

(Lobo et al., 2020). The SARPs for nvPM specify standardized sampling and measurement protocols (SAE, 2013, 2018; ICAO, 2017), which have been extensively evaluated and validated (Lobo et al., 2015b, 2020; Kinsey et al., 2021). The nvPM regulatory limits are applicable for type certification of aircraft engines, but they do not address the vPM which may have substantial environmental impacts.

To reduce CO_2 emissions, mitigate environmental impacts, and make the aviation sector more sustainable, a significant effort is underway to develop and deploy sustainable aviation fuels (SAFs). Various feedstocks and different conversion pathways can be used to produce SAFs (Hileman and Stratton, 2014), which differ in chemical and physical properties compared to conventional petroleum jet fuel (Vozka et al., 2019), most notably by lacking aromatic and sulfur species that are precursors to nvPM and vPM emissions. New SAF candidates must undergo a rigorous qualification and approval process (ASTM D4054) prior to being certified under the ASTM D7566 standard specification as a blending component. Currently, the ASTM D7566 standard allows SAF blend ratios of up to 50% with conventional fuel for drop-in fuels (Wilson et al., 2013).

The combustion of neat SAFs and blends with conventional jet fuel has been shown to result in different PM emissions characteristics as a function of engine type and operating condition (Beyersdorf et al., 2014; Brem et al., 2015; Corporan et al., 2011; Lobo et al., 2011, 2015a, 2016; Moore et al., 2017; Schripp et al., 2018, 2019; Timko et al., 2010). In addition to changes in PM mass- and number-based emissions, SAF combustion results in changes to particle size distributions (PSD) (Beyersdorf et al., 2014; Cain et al., 2013; Kinsey et al., 2012; Lobo et al., 2011, 2015a, 2016; Schripp et al., 2018; Timko et al., 2010), chemical composition (Elser et al., 2019; Kinsey et al., 2012; Timko et al., 2013; Williams et al., 2012), morphology (Huang and Vander Wal, 2013; Kumal et al., 2020; Liati et al., 2019), hygroscopic properties (Trueblood et al., 2018), and optical properties (Elser et al., 2019).

The standardized sampling and measurement protocol for aircraft engine nvPM emissions was designed and validated for engine certification tests using conventional jet fuel. The SARPs require that number-based nvPM emissions are measured with a butanol-based condensation-nuclei counter with a 50% cut-off size of, at most, 10 nm sampling in single-particle-counting mode downstream of a diluter and catalytic stripper. For mass-based nvPM emissions, the instrument must be insensitive to vPM and able to meet performance specifications for repeatability, zero drift, linearity, limit of detection, rise time, sampling interval, accuracy, and applicability. Limited information is available on aircraft engine nvPM emissions characteristics measured with the standardized system for different engine types burning SAFs and blends with conventional fuel (Durand et al., 2021; Elser et al., 2019; Lobo et al., 2015a, 2016).

The standardized system components are not easily adaptable for use on aircraft for measurement of cruise level nvPM emissions. Consequently, there are no comparable in-flight engine-emissions data available for developing and validating models that predict cruise nvPM-emissions based on engine certification data. Particle size distribution measurements are also not included in the standardized system, which are important for assessing the effects of fuels, operating conditions, and engine technologies on the environmental impacts of PM emissions. Thus to advance our understanding of aircraft engine emissions and the factors that control them as well as to develop a large and consistent observational data base, it is important to evaluate the relative performance of other diagnostic instruments that are not prescribed in the standardized protocol but meet these needs. Such instruments must be evaluated for their response to nvPM and total PM emissions from aircraft engines using standardized and non-standardized systems, and for measurements at the engine exit plane and downstream of the engine in the near field, since these instruments are typically used with minimal change to their operating parameters for a wide range of sampling conditions. Very limited data are available in the literature for this purpose, and no data have yet been published for SAFs.

Deleted: s

Deleted: 50% cut-size

Deleted: To date, the only commercial instruments that satisfy the SARPs number and mass measurement system requirements, respectively, are the AVL Particle Counter (APC) Advanced, and the AVL Micro Soot Sensor (MSS) and the Artium Laser Induced Incandescence LII 300 instrument (LII).

Deleted: ¶
¶

Moved down [1]: The observations presented in this paper were collected during the NASA/DLR-Multidisciplinary Airborne Experiment (ND-MAX)/ Emission and Climate Impact of Alternative Fuel (ECLIF) 2 campaign that was conducted at Ramstein Air Base, Ramstein-Miesenbach, Germany in January-February 2018 (see overview by (Anderson and NDMAX-Team, 2021)). The campaign included ground-based and in-flight measurements of emissions from the DLR Advanced Technology Research Aircraft (ATRA) A320 aircraft with V2527-A5 engines running on two conventional jet fuels and three blends with SAF. The main objective of the ground-based measurements was to characterize the nvPM, total PM, and hydrocarbon emissions as functions of engine thrust condition and fuel composition. Several identical instruments were included in the in-flight sampling aircraft (NASA DC-8) and ground measurement diagnostic instrument suites to enable comparisons of engine emissions during ground and airborne operations, and create a data set for testing cruise emission models. The NASA DC-8 aircraft with CFM56-2C1 engines was also used as an emissions source to compare various emissions diagnostic instruments during the ground-based measurements. ¶

184 Here, we present the inter-comparison of real-time measurements of aircraft
185 engine nvPM emissions in terms of physical characteristics such as mass, number,
186 and size distributions using different diagnostic instruments and measurement
187 principles. The nvPM mass emissions were evaluated using three real-time
188 measurement techniques: photoacoustic spectroscopy, the extinction-minus-
189 scattering technique, and laser-induced incandescence (LII), and two alternative
190 measurement techniques widely used in laboratories and on-board aircraft: filter-
191 based photometry and PSD integration. We note that one of the photoacoustic
192 instruments and the LII instruments have been demonstrated to be compliant with
193 the ICAO SARPs performance specifications. The PM number-based emissions
194 were measured using a condensation particle counter. The PSD characteristics
195 measured by scanning mobility particle sizers and an electrical mobility
196 spectrometer were also compared. The nvPM and total PM emissions were
197 delineated using a thermal denuder and a catalytic stripper. We also report the
198 effect of laser fluence on the laser-induced incandescence of nvPM for SAF
199 combustion as changing carbon nanostructure is known to influence particle light
200 absorption and consequently LII signals, and hence the derived nvPM mass
201 concentration. The impact of fuel composition on PM emissions will be reported
202 separately (Schripp et al., 2022).

3 Methods

204 The observations presented in this paper were collected during the NASA/DLR-
205 Multidisciplinary Airborne Experiment (ND-MAX)/ Emission and Climate Impact
206 of Alternative Fuel (ECLIF) 2 campaign that was conducted at Ramstein Air Base,
207 Ramstein-Miesenbach, Germany in January-February 2018. The campaign included
208 ground-based and in-flight measurements of emissions from the DLR Advanced
209 Technology Research Aircraft (ATRA) A320 aircraft with V2527-A5 engines
210 running on two conventional jet fuels and three blends with SAF. The main
211 objective of the ground-based measurements was to characterize the nvPM, total
212 PM, and hydrocarbon emissions as functions of engine thrust condition and fuel
213 composition. Several identical instruments were included in the in-flight sampling
214 aircraft (NASA DC-8) and ground measurement diagnostic instrument suites to
215 enable comparisons of engine emissions during ground and airborne operations.

and create a data set for testing cruise emission models. The NASA DC-8 aircraft with CFM56-2C1 engines was also used as an emissions source to compare various emissions diagnostic instruments during the ground-based measurements.

3.1 Engine and fuels

In the majority of this work, emissions were sampled from a single IAE mixed-flow V2527-A5 starboard engine of the DLR ATRA aircraft (Airbus A320-232). The engine was operated on two conventional, petroleum jet fuels, referred to as REF3 and REF4, and three sustainable aviation fuel blends, referred to as SAF1, SAF2, and SAF3. The abbreviations for the two conventional petroleum fuels are used to avoid confusion with the previous ECLIF campaign (Schripp et al., 2018).

A limited number of experiments were also performed with JP-8 fuel, combusted in the starboard CFM56-2C1 engine (#3) of the NASA DC-8 aircraft. Due to limited fuel availability, none of the other five fuels could be combusted in the CFM56-2C1 engine. The properties of the six fuels are summarized in Table 1.

3.2 Ambient conditions

The measurements presented here were performed outdoors during winter in western Germany. Detailed meteorology for each test point is given in the supplement. The minimum, median, and maximum temperatures were 2.3, 2.9, 8.3 °C, respectively. Conditions were humid (>83 % humidity) and sometimes rainy. Winds ranged from 0 to 15.5 km h^{-1} and wind direction was sometimes variable. The median wind direction was south-westerly, while the source aircraft was oriented facing to the east. Consequently, winds blowing approximately 45° angle from the right rear of the source aircraft sometimes prevented the engine emissions from reaching the sampling probe at low engine thrust settings.

3.3 Emissions sampling

An extensive suite of aerosol and gas-phase instruments operated by the members of six different institutions were deployed in two different shipping

Deleted: in this manuscript

containers to characterize the emissions (Table 2). The complete emission-sampling setup is discussed in a companion paper (Schripp et al., 2022). Briefly, emissions were sampled through a probe located 43 m downstream of the starboard engine of the aircraft. The probe was placed in front of a blast fence located on the western side of the Ramstein Air Force Base flight line, and the fence redirected the engine exhaust upwards for safety. The probe was connected to a 18.5-mm ID, 20-m-long electrically-conductive sampling line heated to 60 °C, that transported flow to a sampling plenum maintained at 33 °C. To minimize residence time and particle losses in this sampling line, a pump ensured that a total of at least 137 L min^{-1} flowed through the sampling manifold at all times. Higher flows produce an unacceptably large pressure drop in the primary sampling line. The majority of this flow was discarded as excess.

The plenum was placed inside a modified shipping container (Container 1) behind the blast fence, along with the NRC, DLR, and NASA instruments. The North American Reference System (NARS) was connected to the plenum by a short section of heated line to the NARS dilutor box, which was heated to 60 ± 15 °C and contained a custom Dekati dilutor with a dilution factor of approximately 4 (less than the standard Dekati dilutor factor of 8 to 14). A 25 m line heated to 60 ± 15 °C transferred sample aerosols flow from the dilutor box to a second shipping container (Container 2), where the MST and ARI instruments were connected. The NARS components include the 25 m heated line, attached diluters and MST instrument suite; the system is compliant with specifications for the standardized nvPM sampling and measurement system (SAE, 2013; SAE, 2018; ICAO, 2017) and whose performance has been demonstrated and evaluated in previous studies (Lobo et al., 2015b, 2016, 2020). Additional instrumentation installed as part of the NARS included a fast electrical mobility spectrometer (Cambustion DMS500), an Aerodyne Aerosol Mass Spectrometer (results not presented here), and a CAPS PMssa monitor (Aerodyne Research Inc.). The details of the instruments installed inside these two containers are listed in Table 3.

Deleted: s

Deleted: (Anderson and NDMAX-Team, 2021;

Deleted: and NDMAX-Team

Deleted: 2021

Deleted: ratio

Deleted: ratio

Deleted: in parallel

3.3.1 Gaseous measurements

A suite of gaseous emissions was measured in this study, as summarized in Table 2. The CO_2 measurements from the NASA LI-COR 7000 were in good agreement with those taken by DLR (MKS MultiGas 2030 FTIR Continuous Gas Analyzer) and MST (LI-COR model 840A), but had a faster response time and were therefore used as the reference for instruments in Container 1. Instruments in Container 2 used the MST measurements as reference.

3.3.2 nvPM number and particle size distributions (PSDs)

nvPM number concentration was measured directly by a certification-test-compliant, particle counter, APC (AVL Inc., which contains a TSI Model 3790E CPC), which was part of the NARS in Container 2. PSDs were measured with two technologies: scanning mobility particle sizers (SMPS, TSI Inc.) and electrical mobility sizers (EMS). Two types of EMS were used; the Cambustion DMS500 (in Container 2, measuring particles 5 to 1000 nm in diameter; data processed with a bimodal calibration matrix and log-normal inversion) and the TSI Engine Exhaust Particle Sizer (EEPS, Container 1, measuring particles from 6 to 523 nm). However, the EEPS data were excluded from this analysis due to unidentified problems with the instrument which led to anomalous PSDs.

Two SMPSs measured nvPM PSDs. An SMPS operated by NRC measured particles 10 to 278 nm in diameter downstream of a catalytic stripper (Model CS015, Catalytic Instruments GmbH), which heated samples to 350 °C before oxidizing gas-phase VOCs to prevent them from recondensing after exiting the device. Another SMPS operated by NASA measured particles 10 to 278 nm in diameter either directly or downstream of a NASA-constructed thermal denuder (TD) also operated at 350 °C. The TD employs a concentric activated charcoal filter downstream of the sample heater to prevent re-condensation of volatile species. TDs are commonly used on-board aircraft for measuring nvPM number concentration and size distributions (Clarke, 1991; Moore et al., 2017) and have been shown to effectively evaporate nucleation and accumulation mode sulfate and organic aerosols (Beyersdorf et al., 2014; Schripp et al., 2018).

Deleted: 10

3.3.3 nvPM mass measurements

In this study, most of the nvPM mass data were derived from light absorption coefficients (units of m^{-1}), either determined in flow-through sample cells (the CAPS PM$_{SSA}$, PAX, and MSS introduced below) or after collecting particles onto a filter (the TAP and PSAP introduced below). Such absorption measurements can be converted to equivalent black carbon or eBC mass concentrations (eBC, units of $g\,m^{-3}$; Petzold et al. (2013)) by dividing them by a reference mass absorption cross-section (MAC, units of $m^2\,g^{-1}$). The LII measurements also rely on light absorption, although the measurand is not absorption but incandescence at two wavelengths and is termed rBC (Petzold et al., 2013; Michelsen et al., 2014).

The reference MAC used to report eBC represents an assumed physical property of the nvPM emitted by the engine at a given time. The extensive review of Bond and Bergstrom (2006) concluded that the MAC at 550 nm of externally-mixed BC from a variety of sources could be summarized as $7.5 \pm 1.2\,m^2\,g^{-1}$; the more recent review of in-situ measurements by (Liu et al., 2020) recommended $8.0 \pm 0.7\,m^2\,g^{-1}$ at 550 nm. In this study, we have used the Bond and Bergstrom value of $7.5\,m^2\,g^{-1}$ for consistency with earlier work and instrument software. These values are assumed to vary inversely with wavelength, with an Angstrom (power) exponent of 1; for example, the 660 nm CAPS PM$_{SSA}$ monitor data were processed with a MAC of $7.5\,m^2\,g^{-1} \times (550\,nm\,/\,660\,nm)^1 = 6.5\,m^2\,g^{-1}$.

One eBC technique, the CAPS PM$_{SSA}$ monitor (Aerodyne Research Inc.; Onasch et al., 2015) derives absorption coefficients as the difference between measured aerosol extinction and scattering coefficients, from which eBC concentrations were calculated as described above. The CAPS PM$_{SSA}$ measures light extinction by the calibration-free cavity attenuation phase shift (CAPS) technique and light scattering with an integrating nephelometer. The CAPS technique measures the lifetime of photons in a high-finesse optical cavity comprised of two high reflectivity mirrors, from which the extinction coefficient can be calculated. An integrating nephelometer captures light scattered from a section of this cavity, and is calibrated using the measured extinction of small (Rayleigh regime) non-absorbing particles. In this study, two CAPS PM$_{SSA}$ monitors were present, one operated at 630 nm wavelength by ARI and the other at 660 nm wavelength by

NRC. The scattering channel of the NRC CAPS PM$_{SSA}$ was calibrated on-site using nebulized and dried ammonium sulfate particles; the other instruments were similarly calibrated prior to the campaign at the manufacturer using 200 nm ammonium sulfate. For the sub-200 nm particles measured in this study, no truncation corrections (Modini et al., 2021) were necessary.

Two other eBC instruments were based on photoacoustic spectroscopy, namely the Photoacoustic Extinctiometer (PAX, DMT Inc,; Nakayama et al., 2015) and the Micro Soot Sensor (MSS; AVL GmbH; Schindler et al., 2004). In both of these instruments, aerosol absorption is measured by the periodic heating of particles using a modulated laser, resulting in the generation of pressure waves which are amplified by an acoustic cell and detected by a microphone. The PAX was calibrated using nebulized ammonium sulfate as well as graphitic nanoparticles (Aquadag).

During on-site calibration of the PAX using graphitic Aquadag nanoparticles, the PAX signals were observed to drift slowly upwards after each baseline. We were nevertheless able to obtain useful data by configuring the PAX to auto-baseline every 180 seconds, and only using the first 15 seconds of measurements after each baseline. After the campaign, it was found that a component of the circuit board was damaged during the initial shipment. In spite of this electrical problem, the PAX data do not represent outliers in the following analysis.

Two additional pairs of eBC instruments were deployed at the ground site and on-board the NASA DC-8 that measured aerosol absorption coefficients based on filter attenuation, namely a Particle Soot Absorption Photometer (PSAP, Radiance Research; Bond et al., 1999) and Tricolor Absorption Photometer (TAP, Brechtel Manufacturing Inc, ; Ogren et al., 2017). These instruments were designed as low-cost, low-maintenance devices for monitoring aerosol optical properties in the background atmosphere (i.e., at low concentrations) and have been used previously in airborne and ground-based studies (Moore et al., 2017). In these instruments, particles are continuously collected onto an internal filter while its light attenuation is measured. The change in light attenuation over time is used to calculate absorption coefficients. This calculation requires post-processing to

Deleted: ed

correct for filter loading effects (which do not require independent measurements) and may also be corrected for light attenuation due to scattering rather than absorption (which requires an independent nephelometer measurement) (Virkkula, 2010). Other sources of error include nonlinearities due to size-dependent penetration of particles into the filter media and the evaporation of volatile species over time (Lack et al., 2014; Nakayama et al., 2010). We note that the TAP automatically advances its filter when its transmission drops below 80%, whereas the PSAP requires a manual filter change. The PSAP filter was therefore changed manually before each set of experiments herein, to ensure that its filter transmission remained above 80% during all measurements.

Three Artium LII 300 (Artium Technologies) instruments measured rBC, based on two-colour pulsed laser–induced incandescence (LII) (Snelling et al., 2005). These instruments heat nvPM using a 1064 nm pulsed laser and measure the resulting incandescence at two wavelength bands. From this measurement, rBC temperature and mass concentrations can be calculated. One of the LII 300s was a component of the NARS. Of the other two, one was dedicated to an experiment where its operating conditions were varied (Section 4.6). Therefore, only two LII 300s were measuring real-time nvPM mass concentration simultaneously at any given time. The MSS+ and the LII 300s were calibrated by reference to the elemental carbon mass (defined by thermal–optical analysis) produced by a laboratory diffusion-flame combustion aerosol source using measurements at three mass concentrations spanning 0.1 to 0.5 mg m^{-3} (SAE, 2018).

Finally, the SMPS PSDs were converted to equivalent mass concentrations by the integrated PSD approach, described in detail by Momenimovahed and Olfert (2015). In brief, the equivalent mass of each SMPS-reported mobility diameter was calculated using an effective density of 1000 kg m^{-3}, which has been shown to produce better than 20% accuracy relative to more complete, size-resolved effective densities (Durdina et al., 2014).

3.4 Data analysis

3.4.1 Emission index calculations

The raw data were analysed over comparable time intervals and cross-checked by independent calculations. The general analysis proceeded as described in this section. First, the time series of measured CO_2 concentrations was used as a reference against which to synchronize all time series, based on rapid rises and falls in the observed concentrations (measured at 1 Hz) when the engine thrust condition underwent large changes (as shown at 08:00 in Figure 2). All instruments were synchronized against the NASA CO_2 sensor except the instruments in container 2, which was synchronized against the MST LI-COR CO_2 sensor, because of the additional dilution stage. The time synchronization accounted for different lag times due to differences in the response times and clock accuracy of each instrument.

Second, the CO_2 concentrations [CO_2] were baseline-subtracted and filtered as follows. The CO_2 baseline ([CO_2]$_b$) was calculated as the mean of the CO_2 concentrations measured before ([CO_2]$_0$) and after ([CO_2]$_1$) each test. The uncertainty in this baseline value was calculated as either ([CO_2]$_b$ – [CO_2]$_0$) or ([CO_2]$_b$ – [CO_2]$_1$), whichever was greater.

Due to the prevailing crosswind mentioned above, unstable CO_2 concentrations occurred during some test points at the idle engine thrust condition. These unstable conditions were identified and filtered using two separate methods. In the first method, the SMPS PSDs were inspected for reproducibility. In the second method, an algorithm was used to reject any test points with CO_2 uncertainties greater than 50%, CO_2 signals less than a factor of ten greater than uncertainty, or CO_2 signals less than 20% above baseline. We found that the first method rejected all of the points rejected by the algorithm, in addition to a few additional points. The analysis presented uses the first method.

Third, all data were arithmetically averaged over the test point periods defined in Table S1. For each instrument, the averaging periods were refined by inspection of the data since sampling-line residence times varied. The averaged data were

444 typically at 1 Hz sampling frequency initially, although the SMPS instruments

445 measured PSDs at 45 second intervals (NRC instrument) or 30 second intervals

446 (NASA). Emission indices (EIs) were then calculated from the averaged data

447 following (SAE, 2013):

$$EI_m = PM_m \frac{RT_m}{[CO_2](M_c + \alpha M_H)P_m} \qquad (1)$$

448

$$EI_{num} = PN \times 10^6 \frac{RT_m}{[CO_2](M_c + \alpha M_H)P_m} \qquad (2)$$

449

450 Where EI_m and EI_{num} are mass and number-based EIs, respectively; PM_m

451 and PN are mass and number concentrations, respectively, at standard reference

452 temperature (T_m; 273.15 K) and pressure (P_m; 1 atm); α is the hydrogen to carbon

453 ratio of the fuel; M_c and M_H are the molar masses of carbon and hydrogen,

454 respectively; and R is the ideal gas constant (0.082 L.atm.K^{-1}.mol^{-1}).

455 3.4.2   Penetration correction

Deleted: Loss

456 Particles may be lost to the walls of sampling lines or to deposits on those

457 walls. The fraction of particles penetrating a given system varies with size,

458 according to a characteristic penetration function. Four penetration functions were

459 applied in this study: 1) from the probe to the sampling plenum, 2) from the

460 plenum to the NARS, 3) within the TD, and 4) within the CS (Figure 4). Function 1

461 was measured on site as described below. Function 2 was calculated using the

462 standard equations for line penetration, as detailed in the loss calculation

463 methodologies provided in SAE documents AIR6504 (SAE, 2017) and ARP6481

464 (SAE, 2019). Function 3 was experimentally determined in the laboratory by

465 NASA. Function 4 was obtained from theoretical estimates and experimental

466 measurements (Catalytic Stripper manual, 2014).

467

468 Penetration function 1 (probe-to-plenum penetration) was measured

469 experimentally by nebulizing ammonium sulfate particles at the probe while all

470 instruments were sampling and all heated lines had reached thermal equilibrium.

471 (Function 1 therefore also includes the smaller instrument sampling lines

downstream of the plenum in its correction as well; however, these were considered negligible relative to the longer probe-to-plenum and plenum-to-Container-2 transport lengths.) For this measurement, the NRC SMPS was moved to the probe, while the NASA instrument remained in its standard position. The ratio of the NASA to NRC PSDs (GMD 30 nm, GSD 1.7) then provided a first estimate of the penetration function. However, this first estimate was not accurate, as the measurements were performed on a cold day (measured as approximately 5 °C outdoors and 15 °C in the instrument container) and as it does not account for performance differences between the NASA and NRC SMPSs. Therefore, two corrections were made. First, both measurements were corrected to standard temperature and pressure. Second, differences between the two instruments were directly measured by moving the NRC SMPS just outside of the sampling container (to keep it at 5 °C) and connecting it to an identical sampling line as the NASA SMPS. The ratio of the two measured PSDs in this setup was defined as equal to unity at all sizes, and used to correct the initial penetration function. Therefore, no further correction was made for sampling lines in Container 1. Losses in this additional line were negligible (calculated penetrations of 0.997 at 100 nm and 0.98 at 20 nm) relative to the long NARS line to Container 2 (i.e., Function 2).

All reported data are corrected for these penetration functions. Size-resolved data (SMPS) were corrected using the size-resolved penetration functions shown in Figure 4. Size-integrated data (all other instruments) were corrected by weighting the penetration functions by the corresponding measured SMPS PVDs. The correction factors are given in the Data Availability section.

3.5   Uncertainties

All reported uncertainties and error bars represent standard errors, propagated through the calculation as necessary. When two independent sources of uncertainty were available (for example, the standard error in the 10 second averages of $[CO_2]$ and the uncertainty in the baseline value) they were added in quadrature. Our bottom-up calculations of uncertainty can be compared with the spread of the data points in our EI comparisons below. This spread represents a

505 top-down uncertainty, and is similar in magnitude to the bottom-up uncertainties
506 (i.e. error bars). This similarity lends confidence to our uncertainty estimates. In
507 most figures, error bars have generally been omitted for clarity, but uncertainties
508 are given for each instrument at each test point in Table S1.

509 ## 4   Results and discussion

510 ### 4.1   Experiment overview

511 A typical time series obtained when the emissions from the IAE V2527-A5 engine
512 were sampled is shown in Figure 2. Nominal low-pressure turbine fan speeds (N1)
513 expressed as a percentage of maximum continuous thrust, are shown by the labels
514 at the top of the figure. Percent N1 (along with engine fuel flow rate) is another
515 metric for representing the different engine thrust conditions and is used as a
516 primary independent variable in this study. The CO_2 concentrations (red line) were
517 highly variable at N1 = 23% as the ambient wind shifted the aircraft exhaust plume
518 toward and away from the sampling probe. Correspondingly, both nvPM mass and
519 PSD measurements were highly variable, as shown by the blue trace and black
520 symbols, respectively.

521

522 As shown in Figure 3a, nvPM mass concentrations, represented by EI_m, increased
523 with increasing N1 before decreasing slightly at the highest N1, similar to the
524 trends for other engine types reported by Lobo et al. (2015b, 2020). Figure 3b
525 shows that the relationship for EI_{num} is less clear, with a slight increase at
526 moderate N1 followed by a greater decrease at high N1. As discussed below
527 (Section 4.2.3), the higher EI_m at higher N1 thrust was associated with larger
528 particle sizes, and therefore smaller penetration-function corrections (Section
529 4.2.1). Finally, for context, Figure 3c shows the relationship of the PM mass
530 concentrations, used to calculate EI_m (based on the geometric mean EI_m discussed
531 in Section 4.4.1), with baseline-subtracted CO_2 concentrations from the measured
532 plume. An effect of fuel composition is evident, and discussed in detail in Schripp et
533 al. (2022).

Formatted: Subscript

Deleted: (Schripp and NDMAX-Team, 2021)

4.2 Size distributions and penetration functions

4.2.1 Penetration function

A typical PSD, and corresponding PVD, are shown in Figure 4, in the context of the penetration functions applied in this work. The PVD was calculated by assuming spherical particles, which incurs negligible error for aircraft-engine nvPM due to the small diameter of particles produced by such engines (Durdina et al., 2014; Saffaripour et al., 2020). For the example PSD and PVD in Figure 4 (shading), it is clear that a substantial fraction of the particle number was corrected for penetrations (lines) of roughly 0.5. In contrast, the larger mode of the PVD corresponds to penetrations larger than 0.8 in most cases. These differences led to a median number- and mass-based correction factors of 1.51 and 1.19, respectively for penetration Function 1 (probe to plenum) labelled in the figure. The remaining instrument-specific penetration corrections were applied according to the position of each instrument in the sampling system, as specified in Table 2. The magnitude of each correction is given in Table S1.

4.2.2 PSDs

Figure 5 shows selected PSDs from the IAE V2527-A5 engine operated with SAJF1 (Figure 5a) and REF4 (Figure 5b) fuels. The PSDs are corrected for line penetration as described above. The plot illustrates a lower (40 % N1) and a higher thrust point (60 % N1) from the available data for two fuels. Note that the ordinate scales are harmonized across the upper and lower rows only. All abscissa scales are harmonized. The figure indicates roughly comparable PSDs from these two fuels. The companion paper (Schripp et al., 2022) compares the effects of fuel composition in detail.

The CFM56-2C1 engine on the DC-8 burning JP-8 emitted an order of magnitude more total particles per unit fuel burned than any of the fuels combusted in the ATRA (data not shown). We attribute this difference to the relatively high sulfur content of the JP-8 fuel (1490 ppm sulfur versus ≤ 105 ppm for the other fuels). The CFM56-2C1 engine also emitted a factor of three lower nvPM mass and nvPM number than the V2527-A5 engine.

Markup in margin (track changes):
Moved down [2]: Figure 5 shows selected PSDs from the IAE V2527-A5 engine operated with SAJF1 (Figure 5a) and REF4 (Figure 5b) fuels. The plot illustrates a lower (40 %) and a higher thrust point (60 %) from the available data for two fuels. Note that the ordinate scales are harmonized across the upper and lower rows only. All abscissa scales are harmonized. The figure indicates roughly comparable PSDs from these two fuels. The companion paper (Schripp and NDMAX-Team, 2021) compares the effects of fuel composition in detail.¶
Deleted:
Deleted:
Deleted:
Deleted: of CFM56-2C1
Moved (insertion) [2]
Deleted: and NDMAX-Team
Deleted: 1

582 The presence of extremely small particles with $d_m <$ 10nm was evident in the two
583 nvPM PSDs (not shown due to the extremely large penetration function at these
584 sizes; Figure 4). The CS-SMPS data extended to smaller diameters, and showed that
585 the size range measured by these two instruments was insufficient to capture the
586 full PSD for the CFM56-2C1 engine data at 22% N1 as well as 63% N1. The $d_m <$
587 10nm mode was not as prominent in the V2527-A5 engine exhaust at any thrust,
588 although some evidence was observed for it (e.g. number distribution at 40% N1 in
589 Figure 5b). Our data do not allow us to identify whether these small particles were
590 non-volatile or represent an imperfect performance of the CS and TD.

591

592 There is some evidence for an increase in SMPS-calculated volume at larger
593 particle sizes in Figure 5a, at both 40% and 60% N1. If these large particles
594 indicated the presence of a large aerosol mode which varied independently from
595 the primary mode (e.g. if they were emitted by some other process than the engine
596 itself), they would introduce a EI_m-dependent bias in the ratio of SMPS-based EI_m
597 to other instruments, which was not observed (Section 4.4.2).

598

599 Since the CFM56-2C1-with-JP-8 data were strongly influenced by a nucleation
600 mode, and were therefore not well described by the GMD and GSD of the data,
601 these measurements have been omitted from all subsequent PSD analysis in this
602 manuscript. Bimodal fits to the data were not possible as the nucleation mode was
603 not captured by our size distributions. However, the nvPM mass measurements
604 are much less sensitive to these small particles (Hinds, 1999) and have therefore
605 been retained. PSDs from all instruments, test points, and fuels from both the
606 CFM56-2C1 and V2527-A5 engines are included in the supplement.

607 4.2.3   Particle size statistics; GMD and GSD

608 Figure 6 summarizes the PSDs measured by three instruments in terms of their
609 GMD and GSD. The data sets labelled SMPS and TD-SMPS were both obtained from
610 NASA's SMPS, which was manually switched to a bypass line and the TD at each
611 test point. The data set labelled CS-SMPS was obtained with NRC's SMPS.

612 Total PM is represented by the data sets labelled DMS500 and SMPS. However, the
613 two are not directly comparable because the DMS500 measurements were
614 obtained after an additional dilution by a factor of 4 in the NARS and the DMS500
615 was not operated behind a volatile particle remover (CS or TD). Moreover, the
616 inversion of DMS500 data requires more assumptions about the particle size
617 distribution than the analogous SMPS calculation. Either volatiles or this inversion
618 procedure may have caused the 10% larger GSDs observed for the DMS500 for
619 some data (some measurements with GMDs over 35 nm) relative to the SMPS.
620 Since volatiles would affect both GMD and GSD, but we primarily observed
621 discrepancies in the DMS500 GSD, we suggest that the inversion was the major
622 source of bias in these data.
623
624 nvPM is represented by the open circles and filled squares in Figure 6. These two
625 data sets show a different relationship (slope) between GMD and GSD, reflecting
626 systematic differences in the corresponding PSDs. Relative to the mean of the two
627 instruments, the NRC GMDs were higher (Figure 7a) while the NRC GSDs were
628 higher at GSD < 1.75 but lower at GSD > 1.75 (Figure 7b). Inspection of the
629 corresponding PSDs showed that the NASA and NRC instruments agreed at higher
630 d_m but that NRC number concentrations were higher at smaller d_m. This trend
631 suggests that a bias in the penetration functions applied to each instrument
632 (Figure 4, Table 2) led to the discrepancy in GMD and GSD. Such a bias would affect
633 the nvPM concentration estimated from these PSDs (Figure 8b) and will be
634 discussed further below.

635 In spite of these trends in GMD and GSD, the PSD measurements agreed to within
636 20% (Figure 7a) for nvPM GMDs and within 5% for nvPM GSDs (Figure 7b).
637 Furthermore, these measurements are consistent with previous measurements by
638 Lobo et al. (2015c), as illustrated by the line in Figure 6, which reproduces the
639 polynomial best-fit line reported by those authors.

4.3 Consistency between number-based emission indices of nvPM and vPM

Figure 7c compares the measured vPM and nvPM EI_{num} with the mean nvPM EI_{num} (i.e., mean of the NRC CS-SMPS, NASA TD-SMPS, and NARS APC. The grey shading shows that all instruments agreed to within a factor of 2. The APC and DMS500 nvPM EI_{num} were both typically higher than the two similar SMPSs. Substantial variability between the two SMPSs was also observed.

In Figure 7c, the penetration-corrected APC EI_{num} are approximately 50% larger than the SMPS EI_{num} under all conditions. Our measured PSDs rule out the possibility that 50% of particles were not seen by the SMPS. Therefore, we attribute the difference between APC and SMPS results to uncertainties in the APC or SMPS penetration correction functions (Figure 4), i.e., we hypothesize that this difference would not have been observed had the instruments all sampled from the same plenum from comparable sampling lines.

We also attribute the larger nvPM EI_{num} measured by the DMS500 to the same cause; to which a similar penetration function as the APC applies (Section 3.4.2). We note that the DMS500 measured total PN, not nvPN, so is expected to report higher number concentrations when volatile particles are present.

4.4 Consistency between mass-based emission indices

4.4.1 EI_m measurements by real-time sampling instruments

Figure 8a presents scatterplots of the real-time EI_m measurements acquired during this study for all fuels and both engine types. In Figure 8a, the individual EI_m are plotted against the geometric mean of the instruments shown in the caption: three LII 300 instruments, two CAPS instruments, one PAX and one MSS+. The geometric mean was chosen over the more-common arithmetic mean because the data are not normally distributed; the arithmetic mean would therefore have over-emphasized outliers.

Figure 9a presents the same data as Figure 8a except that the ordinate data have

690 been normalized to the geometric-mean EI_m from Figure 8a. Most data fall within

691 30 % of the mean (inner dashed lines) above 100 mg / kg_{fuel}. We note that exhaust

692 samples were diluted with background air by a factor of 40 or more before

693 reaching the inlet probe, so at this lower limit, the actual concentration observed

694 by the instruments was approximately 10 μg m^{-3} (the exact conversion factor

695 varies with CO_2 concentration and fuel properties), which is close to their

696 detection limits, as expected. This lower limit may have been influenced by the

697 ambient measurement conditions, where background nvPM concentrations were

698 non-negligible.

699 The agreement of the real-time measurements to within 30 % is larger than the

700 calibration uncertainties of the individual instruments, and suggests an influence

701 of systematic biases (e.g. in instrument calibration or penetration corrections).

702 There is no evidence of systematic differences between absorption and LII

703 measurements, which might have been hypothesized if coatings of volatile PM on

704 the light-absorbing nvPM had enhanced absorption. The larger scatter at lower

705 EIm values reflects the noise levels of the instruments. Both of these observations

706 are consistent with data reported previously for different engine types by Lobo et

707 al. (2016, 2020). The LII 300 and MSS+ from the North American Reference System

708 (NARS) have been widely used to characterize aircraft engine nvPM emissions. The

709 two CAPS instruments were independently calibrated and operated. The MSS+ and

710 PAX represent two photoacoustic spectrometers from different manufacturers,

711 operated by different teams, with different principles of calibration. The PAX was

712 also operated with a damaged capacitor on its printed circuit board. As noted in

713 Methods, these instruments operate on a variety of physical principles, including

714 photoacoustic spectroscopy (with two different designs), extinction-minus-

715 scattering, and laser-induced incandescence (cf. Section 3.3.3). Agreement

716 between these various principles also suggests that factors such as volatile

717 coatings on nvPM did not influence the instrument responses.

718 4.4.2   SMPS-based EI_m

719 Figure 8b and Figure 9b are analogous to Figure 8a and Figure 9a, but for the

720 integrative nvPM measurements that do not fall into the real-time sampling

Deleted: notable considering the different types of instruments used.

723 category. These data are plotted against the same geometric mean from Figure 8a.

724 The dashed lines in Figure 9b represent the same ratios as in Figure 9a.

725 Considering that the real-time instruments in Figure 8a were either calibrated to

726 aerosol absorption or to aviation nvPM, we consider their accuracy as greater than

727 the instruments in Figure 8b and consider departures from the 1:1 line as due to

728 inaccuracy.

729 Most of the instruments in Figure 8b were accurate to within 30% of the reference,

730 similar to Figure 8a, with the exception of the CS-SMPS and PSAP. This is

731 summarized in Table 3, which shows the mean ratios of all data except engine idle

732 (23% N1) with the geometric mean. Table 3 also includes the results of a linear

733 regression against the geometric mean to facilitate comparison of our

734 measurements with Kinsey et al. (2021), who performed linear regressions against

735 simultaneous elemental carbon (EC) measurements (in our study, mass

736 concentrations were too low to obtain EC measurements). The PSAP data are

737 discussed in the next section. The CS-SMPS data were systematically higher than

738 the geometric mean, potentially due to an overcorrection of the penetration of

739 large particles to the SMPS.

740 Since the spread of nvPM EI_m reported by the two SMPS systems was smaller than

741 the bias, their difference relative to the reference EI_m cannot be attributed to

742 measurement biases (such as the limited size range detected by the instruments).

743 Since the two SMPS systems showed different accuracies, their differences cannot

744 be ascribed to a lack of constraints on the effective density of the nvPM particles

745 (Momenimovahed and Olfert, 2015), which may vary with the monomer diameter

746 (Abegglen et al., 2014; Durdina et al., 2014) and/or shape of soot aggregates. (We

747 reiterate that our assumption of constant effective density is expected to introduce

748 negligible uncertainty for the small soot particles emitted by aircraft turbine

749 engines; Durdina et al., 2014). With respect to the real-time measurements, the

750 TD-SMPS data are also consistent with previous measurements of aviation engine

751 PSDs, which, however, were not corrected for diffusional particle loss (Lobo et al.,

752 2015b, 2020). Careful measurement of the penetration functions used in these

753 calculations would be required to confirm our interpretation.

Deleted: imprecision

Deleted: ta

4.4.3 Filter photometer-based EI_m from TAP and PSAP

Figure 8b and Figure 9b show that the TAP measurements were within the 30 % range observed for the real-time instruments, with a relative standard deviation (RSD) of 14 % (Table 3) for all data excluding the engine idle condition (23% N1). This provides high confidence for the use of the TAP for in-flight or field measurements of aircraft-engine nvPM mass emissions, when filter-loading corrections (Section 3.3.3) are correctly applied.

The PSAP, on the other hand, showed much greater variability, with an RSD of 36% (Table 3). This is substantially higher than the variability reported by a laboratory intercomparison of PSAP and CAPS PM_{SSA} (Perim De Faria et al., 2021) (that study did not report a statistic comparable to RSD). Although the PSAP has been observed to deviate up to a factor of two higher in cases of high organic aerosol loading or reduced filter transmission (Lack et al., 2013), our data are restricted to transmissions above 0.8. The fact that the PSAP shows great variability rather than a fixed offset indicates that the issue is not due to a systematic error such as an inaccurate MAC or flow rate calibration.   We note that the TAP and PSAP were operated with reduced sample flow rates of 0.05 L min^{-1} and 0.1 L min^{-1}, respectively, (5 to 10% of nominal settings) to extend the life of their filter media while sampling the high soot concentrations in the aircraft exhaust. Under these conditions, detector noise and small fluctuations in sample flow have a magnified effect on resulting derived absorption coefficients. We suspect that the measurements would have been significantly more precise if the instruments had been operated at nominal flows, although this would have required changing filters after each test point. Consistent with our hypothesis, we note that Nakayama et al. (2010) observed substantially larger variability in PSAP measurements at 0.3 than at 0.7 standard litres per minute. We also note that Bond et al. (1999) did not observe an impact of flow rate when changing from 1 to 2 litres per minute.

Figure 10 plots as a function of particle GMD the same relative TAP and PSAP EI_m data shown in Figure 9b. No clear trend of this ratio with size is evident, although the measurements become somewhat more scattered at smaller sizes for the SAF1

787 data set, where signal to noise is lower (GMD and EI_m were correlated, see the

788 below discussion of Figure 12). Figure 10b includes the size-dependent PSAP

789 correction function reported by Nakayama et al. (2010) (their Equation 8), with

790 shading representing a 1σ uncertainty. Those authors predicted the true

791 absorption values using Mie theory for nigrosin particles of diameter 100 to

792 600 nm and refractive index 1.685−0.285i. Thus, their correction factor is

793 conceptually equivalent to our EI_m/mean-EI_m. Extrapolating their correction

794 function down from 100 nm to 15 nm gives values ranging from 4 to 8, whereas

795 our measurements are close to 1.0. This discrepancy may be attributed primarily

796 to the extrapolation, and possibly also to the fact that we have measured solid

797 nvPM particles rather than liquid nigrosin. Overall, it is clear that the variability in

798 our PSAP data is not sufficiently predicted by the GMD.

799 Overall, our data show that any possible size dependency in the TAP and PSAP

800 response is smaller than the observed variability between samples. The TAP and

801 PSAP data exhibit relative standard deviations (RSD) of 19% and 16%,

802 respectively, for samples with GMD > 25 nm. Future studies may consider

803 correcting PSAP and TAP measurements by the ratios shown in Table 3, which

804 represent the ratio between the calibrated aerosol-phase nvPM mass

805 measurements and the previously uncalibrated PSAP and TAP measurements, for

806 data above 25 mg kg_{fuel}^{-1} and N1 > 40%.

807 4.5   Instrument performance for fuels with different composition

808 Figure 11 shows a category plot of the ratio EI_m/mean-EI_m (that is, the ordinate of

809 Figure 9) for the different instruments. Data below 100 mg / kg_{fuel} have been

810 excluded as this ratio reflects only noise in that region (Figure 9). The symbols

811 have been sized by mean N1. The data have been coded by symbol and colour to

812 reflect the 6 fuels used in this study, although JP-8 measurements are few in

813 number due to the EI_m of the data set (CFM56-2C1 with JP-8) being typically below

814 25 mg / kg_{fuel}.

815 Figure 11 shows that no substantial difference can be seen for these instruments

816 for the nvPM EIm for fuels with different composition; the spread in the data for a

817 given fuel is larger than the difference between fuels. Outliers tend to be associated

818 with low N1 (small symbols). Because low N1 corresponds to both lower

819 concentrations (lower signal-to-noise) and lower exhaust velocities relative to

820 ambient wind speeds, these outliers are not surprising.

821 The instruments in Figure 11 show a linear response to nvPM mass and operate on

822 a range of physical principles. This observation indicates that no instrument was

823 uniquely sensitive to changes in particle size over the observed range, since EI_m

824 was correlated with GMD (Figure 12), as is typical of aviation engines (Saffaripour

825 et al., 2020). We note that the response of all of these instruments is proportional

826 to the MAC of the sample, so that it remains possible that the sample MAC changed

827 with GMD or EI_m.

828 ### 4.6   Influence of LII laser fluence

829 An additional experiment was performed to test the hypothesis that the laser

830 fluence of the LII 300 may not be sufficiently high to heat nvPM to incandescence

831 in aircraft-engine PM emissions from SAFs at different engine thrusts. The

832 experimental design was similar to that of Yuan et al. (2022). This hypothesis is

833 related to electron microscopy evidence (Vander Wal et al., 2014) showing that the

834 degree of graphitization of aircraft-engine soot may be substantially lowered at

835 low thrusts. A lower degree of graphitization may result in a lower LII signal if the

836 1064 nm MAC is lower (resulting in a lower maximum temperature being reached)

837 or if part of the laser energy leads to carbon annealing rather than thermal

838 excitation (Botero et al., 2021; Ugarte, 1992; Vander Wal and Choi, 1999). If

839 correct, this hypothesis would mean that the nvPM concentrations reported by an

840 LII 300 operated at reduced fluence would be lower than those of a reference LII

841 300. Higher fluences are also required for nvPM internally mixed with volatile PM,

842 as some laser energy may be lost to volatile evaporation (Michelsen et al., 2015).

843 Figure 13a illustrates the experiment we performed to test this hypothesis. The

844 figure presents data for SAF1 only; results for other fuels were similar. One

845 "reduced-fluence" LII 300 was programmed to change its Q-switch delay from

846 140 μs to 240 μs, with a randomized order. In this experiment, lower Q-switch

delays corresponded to higher laser fluence; the lowest Q-switch delay was the optimal one for this system. Another "reference" LII 300 operated with no change to its Q-switch delay. Figure 13a shows that the reduced-fluence LII reported lower mass concentrations when its Q-switch delay was increased, but returned to the expected values when its Q-switch delay was reduced.

We defined R_{LII} as the ratio of nvPM mass concentrations reported by the reduced-fluence and reference LII 300 instruments. Figure 13b shows that R_{LII} was a function of Q-switch delay, and therefore laser fluence, for all engine thrust conditions. This observation is expected, since LII signals are lower at lower fluence (Michelsen et al., 2015) and since we calculated R_{LII} without taking this effect into account. We have verified in our laboratory that Q-switch delay is inversely proportional to laser fluence for this system and that saturation effects are negligible.

A trend of decreasing R_{LII} with decreasing N1 is evident at moderate and low Q-switch delays, which can be interpreted as indicating that the nvPM was more graphitic at higher N1 conditions. However, R_{LII} reached a plateau at high fluence (smaller Q-switch delay), which is the region where the LII 300 normally operates. This plateau was reached at all engine thrusts, with a broader range for the plateau at higher thrusts and a decreasing range as the thrust was lowered. Therefore, the LII 300 has sufficient fluence and can be expected to perform well for SAF blends at all engine thrust conditions.

5   Conclusions

For multiple instruments measuring nvPM number, size, and mass, we observed no evidence of anomalous instrument responses to the exhaust emissions produced by SAF blends relative to petroleum jet fuel (REFs) combustion in an IAE V2527-A5 engine. The GMD, GSD, and EI_num data for all fuels fell within 20%, 5%, and a factor of 2 of their mean, respectively. Anomalous instrumental responses would have resulted in two groups of data for these parameters, which was not observed. However, a difference between EI_num for instruments located on different-length sampling lines was noted and attributed to a greater sensitivity of EI_num than EI_m to the penetration function.

Deleted: reference

Deleted: s

880

The majority of nvPM mass measurements by the real-time instruments (CAPS
PM_{SSA}, LII 300, MSS+, PAX) agreed to within 30% of their geometric mean
(reference mean), for EI_m above 100 mg/ kg_{fuel}. This lower limit corresponded to a
mass concentration of approximately 10 µg m^{-3} (the conversion of EI_m to mass
varies because the emitted [CO_2] varies), which was the noise level of these
instruments in our sampling setup. The ratio of each real-time measurement with
the reference mean was close to unity (maximally 1.24, minimally 0.78) and
indicated good precision (all RSDs ≤ 17%).

Integrative nvPM EI_m, calculated from PSD measurements or filter attenuation
(TAP and PSAP), fell within a factor of two of the reference mean. The ratio of each
integrative measurement with the reference mean was further from unity
(maximally 1.50, minimally 0.88) and variability was higher precision (all RSDs
≤ 36%). The variability in TAP data was notably low at 14%, and the variability in
PSAP data was notably high at 36%, likely due to its operation at a reduced flow
rate.

Two other instrument- and fuel composition-specific observations were made. A
dedicated experiment showed that changing the laser fluence of an LII 300 could
influence its reported nvPM mass concentrations at low to moderate fluences. By
maintaining sufficiently high fluence a plateau region was established, irrespective
of thrust or fuel, where reported nvPM mass concentrations were stable and not
influenced by experimental conditions. Second, additional measurements of
emissions from JP-8 fuel combusted in a CFM56-2C1 engine indicated the presence
of very high concentrations of volatile nucleation-mode particles with
diameter < 20 nm. These measurements reflect a different engine, as well as a fuel
with a factor 20 higher sulfur content, and the increased total PM number
concentration is most likely attributable to the sulfur.

Overall, this study found that real-time instruments for the measurement of nvPM
emissions in aviation turbine engines are comparable whether conventional fuels
or SAFs are used. Since all real-time measurements were influenced by the MAC

913   and no independent measurement of nvPM mass was made, no conclusions about

914   the variability thereof can be made from this study.

5.1 Author contributions

BEA, PLC, TS, PL, GJS, PDW, and RML designed the study. JCC, TS, PLC, GJS, ECC, SA, PDW, RML, ZY, AF, MT, DS, WL, CR, PO, MS, and PL took the measurements. JCC, TS, BEA, RHM, MAS, ECC, SA, ZY analyzed the data with input from GJS, PL, RML, and AF. JCC prepared the figures. JCC and PL drafted the manuscript. All authors discussed the data interpretation and presentation.

5.2 Competing interests

RML and AF are employed by ARI, which produces the CAPS PM$_{SSA}$ commercially. ZY was employed by ARI at the time of the study.

5.3 Acknowledgements

We acknowledge the efforts of the flight and ground crews of the DLR ATRA, the NASA DC8, and the U.S. Air Force 86th Air Wing. We thank the ground staff of Ramstein Air Base for their operational support during this experiment.

5.4 Financial support

This research received funding from the Transport Canada project "TC Aviation — nvPM from renewable and conventional fuels". The campaign was funded by the DLR aeronautics program in the framework of the project "Emission and Climate Impact of Alternative Fuels (ECLIF)". MS&T and ARI received support from the U.S. Federal Aviation Administration (FAA) through the Aviation Sustainability Center (ASCENT) – a U.S. FAA-NASA- U.S. DoD-Transport Canada- U.S. EPA sponsored Center of Excellence for Alternative Jet Fuels and Environment under Grant No. 13-C-AJFE-MST, Amendment 010. A.F. was supported by funds from ARI. ATRA operational and fuel costs along with DLR scientists' participation was funded by the DLR aeronautics program in the framework of the project "Emission and Climate Impact of Alternative Fuels (ECLIF)". The U.S. FAA Office of Environment and Energy and the National Aeronautics and Space Administration Aeronautics Research Mission Directorate supported field and DC-8 operations, and participation of the U.S. researchers in the project.

5.5 Data availability

The data presented in Figures 4 to 10 are available in the Zenodo repository at
https://sandbox.zenodo.org/record/950512 as a spreadsheet file. Other data are
available from the authors upon request.

6 References

ASTM D4054: Practice for Evaluation of New Aviation Turbine Fuels and Fuel Additives. Conshohocken, PA: ASTM International; 2019. doi: 10.1520/D4054-19.

ASTM D7566: Specification for Aviation Turbine Fuel Containing Synthesized Hydrocarbons. Conshokocken, PA: ASTM International; 2020. doi: 10.1520/D7566-20

International Civil Aviation Organization (2017). International Standards and Recommended Practices – Annex 16 to the Convention on International Civil Aviation: Environmental Protection, Volume II - Aircraft Engine Emissions, 4th ed., Montreal, QC, Canada.

Abegglen, M., Durdina, L., Mensah, A., Brem, B., Corbin, J., Wang, J., Lohmann, U. and Sierau, B.: Effective density measurements of fresh particulate matter emitted by an aircraft engine, in EGU General Assembly Conference Abstracts, vol. 16, p. 14367., 2014.

ASTM D4054: Practice for Evaluation of New Aviation Turbine Fuels and Fuel Additives. Conshohocken, PA: ASTM International; 2019. doi: 10.1520/D4054-19.

ASTM D7566: Specification for Aviation Turbine Fuel Containing Synthesized Hydrocarbons. Conshokocken, PA: ASTM International; 2020. doi: 10.1520/D7566-20

Beyersdorf, A. J., Timko, M. T., Ziemba, L. D., Bulzan, D., Corporan, E., Herndon, S. C., Howard, R., Miake-Lye, R., Thornhill, K. L., Winstead, E., Wey, C., Yu, Z. and Anderson, B. E.: Reductions in aircraft particulate emissions due to the use of Fischer-Tropsch fuels, Atmos. Chem. Phys., 14(1), 11–23, doi:10.5194/acp-14-11-2014.

Bond, T. C. and Bergstrom, R. W.: Light absorption by carbonaceous particles: An investigative review, Aerosol Sci. Technol., 40(1), 27–67, doi:10.1080/02786820500421521, 2006.

Bond, T. C., Anderson, T. L. and Campbell, D.: Calibration and Intercomparison of Filter-Based Measurements of Visible Light Absorption by Aerosols, Aerosol Sci. Technol., 30(6), 582–600, doi:10.1080/027868299304435, 1999.

Botero, M. L., Akroyd, J., Chen, D., Kraft, M. and Agudelo, J. R.: On the thermophoretic sampling and TEM-based characterisation of soot particles in flames, Carbon N. Y., 171, 711–722, doi:10.1016/j.carbon.2020.09.074, 2021.

Brem, B. T., Durdina, L., Siegerist, F., Beyerle, P., Bruderer, K., Rindlisbacher, T., Rocci-Denis, S., Andac, M. G., Zelina, J., Penanhoat, O. and Wang, J.: Effects of Fuel Aromatic Content on Nonvolatile Particulate Emissions of an In-Production Aircraft Gas Turbine, Environ. Sci. Technol., 49(22), 13149–13157, doi:10.1021/acs.est.5b04167, 2015.

Cain, J., Dewitt, M. J., Blunck, D., Corporan, E., Striebich, R., Anneken, D., Klingshirn, C., Roquemore, W. M. and Vander Wal, R.: Characterization of gaseous and particulate emissions from a turboshaft engine burning conventional, alternative, and surrogate fuels, Energy Fuels, 27(4), 2290–2302, doi:10.1021/ef400009c, 2013.

Catalytic Stripper CS015 Instrument Manual, Catalytic Instruments GmbH, 2014.

Deleted: Anderson, B. E. and NDMAX-Team: Overview of the NASA/DLR Multidisciplinary Airborne Experiment (ND-MAX), in prep., 2021.¶

988 Clarke, A. D.: A thermo-optic technique for in situ analysis of size-resolved aerosol
989 physicochemistry, Atmos. Environ. Part A, Gen. Top., 25(3–4), 635–644,
990 doi:10.1016/0960-1686(91)90061-B, 1991.

991 Corporan, E., Edwards, T., Shafer, L., Dewitt, M. J., Klingshirn, C., Zabarnick, S., West, Z.,
992 Striebich, R., Graham, J. and Klein, J.: Chemical, thermal stability, seal swell, and emissions
993 studies of alternative jet fuels, Energy Fuels, 25(3), 955–966, doi:10.1021/ef101520v,
994 2011.

995 Durand, E., Lobo, P., Crayford, A., Sevcenco, Y. and Christie, S.: Impact of fuel hydrogen
996 content on non-volatile particulate matter emitted from an aircraft auxiliary power unit
997 measured with standardised reference systems, Fuel, 287, 119637,
998 doi:10.1016/j.fuel.2020.119637, 2021.

999 Durdina, L., Brem, B. T., Abegglen, M., Lobo, P., Rindlisbacher, T., Thomson, K. A.,
1000 Smallwood, G. J., Hagen, D. E., Sierau, B. and Wang, J.: Determination of PM mass emissions
1001 from an aircraft turbine engine using particle effective density, Atmos. Environ., 99, 500–
1002 507, doi:10.1016/j.atmosenv.2014.10.018, 2014.

1003 Elser, M., Brem, B. T., Durdina, L., Schönenberger, D., Siegerist, F., Fischer, A. and Wang, J.:
1004 Chemical composition and radiative properties of nascent particulate matter emitted by
1005 an aircraft turbofan burning conventional and alternative fuels, Atmos. Chem. Phys.,
1006 19(10), 6809–6820, doi:10.5194/acp-19-6809-2019, 2019.

1007 Gagné, S., Couillard, M., Gajdosechova, Z., Momenimovahed, A., Smallwood, G., Mester, Z.,
1008 Thomson, K., Lobo, P. and Corbin, J. C.: Ash-Decorated and Ash-Painted Soot from Residual
1009 and Distillate-Fuel Combustion in Four Marine Engines and One Aviation Engine, Environ.
1010 Sci. Technol., 55, 6584–6593, doi:10.1021/acs.est.0c07130, 2021.

1011 Hileman, J. I. and Stratton, R. W.: Alternative jet fuel feasibility, Transp. Policy, 34, 52–62,
1012 doi:10.1016/j.tranpol.2014.02.018, 2014.

1013 Hinds, W. C.: Aerosol technology: properties, behavior, and measurement of airborne
1014 particles, John Wiley & Sons., 1999.

1015 Huang, C. H. and Vander Wal, R. L.: Effect of soot structure evolution from commercial jet
1016 engine burning petroleum based JP-8 and synthetic HRJ and FT fuels, Energy Fuels, 27(8),
1017 4946–4958, doi:10.1021/ef400576c, 2013.

1018 ICAO: International Standards and Recommended Practices – Annex 16 to the Convention
1019 on International Civil Aviation: Environmental Protection, Volume II - Aircraft Engine
1020 Emissions, Montreal, QC., 2017.

1021 International Civil Aviation Organization (2017). International Standards and
1022 Recommended Practices – Annex 16 to the Convention on International Civil Aviation:
1023 Environmental Protection, Volume II - Aircraft Engine Emissions, 4th ed., Montreal, QC,
1024 Canada.

1025 Kiliç, D., El Haddad, I., Brem, B. T., Bruns, E., Bozetti, C., Corbin, J., Durdina, L., Huang, R. J.,
1026 Jiang, J., Klein, F., Lavi, A., Pieber, S. M., Rindlisbacher, T., Rudich, Y., Slowik, J. G., Wang, J.,
1027 Baltensperger, U. and Prévôt, A. S. H.: Identification of secondary aerosol precursors
1028 emitted by an aircraft turbofan, Atmos. Chem. Phys., 18(10), 7379–7391, doi:10.5194/acp-
1029 18-7379-2018, 2018.

1030 Kinsey, J. S., Timko, M. T., Herndon, S. C., Wood, E. C., Yu, Z., Miake-Lye, R. C., Lobo, P.,
1031 Whitefield, P., Hagen, D., Wey, C., Anderson, B. E., Beyersdorf, A. J., Hudgins, C. H., Thornhill,
1032 K. L., Edward, W., Howard, R., Bulzan, D. I., Tacina, K. B. and Knighton, W. B.: Determination
1033 of the emissions from an aircraft auxiliary power unit (APU) during the alternative
1034 aviation fuel experiment (AAFEX), J. Air Waste Manag. Assoc., 62(4), 420–430,
1035 doi:10.1080/10473289.2012.655884, 2012.

Kinsey, J. S., Giannelli, R., Howard, R., Hoffman, B., Frazee, R., Aldridge, M., Leggett, C., Stevens, K., Kittelson, D., Silvis, W., Stevens, J., Lobo, P., Achterberg, S., Swanson, J., Thomson, K., McArthur, T., Hagen, D., Trueblood, M., Wolff, L., Liscinsky, D., Arey, R., Cerully, K., Miake-Lye, R., Onasch, T., Freedman, A., Bachalo, W., Payne, G. and Durlicki, M.: Assessment of a regulatory measurement system for the determination of the non-volatile particulate matter emissions from commercial aircraft engines, J. Aerosol Sci., 154, 105734, doi:10.1016/j.jaerosci.2020.105734, 2021.

Kumal, R. R., Liu, J., Gharpure, A., Vander Wal, R. L., Kinsey, J. S., Giannelli, B., Stevens, J., Leggett, C., Howard, R., Forde, M., Zelenyuk, A., Suski, K., Payne, G., Manin, J., Bachalo, W., Frazee, R., Onasch, T. B., Freedman, A., Kittelson, D. B. and Swanson, J. J.: Impact of Biofuel Blends on Black Carbon Emissions from a Gas Turbine Engine, Energy Fuels, 34(4), 4958–4966, doi:10.1021/acs.energyfuels.0c00094, 2020.

Lack, D. A., Moosmüller, H., McMeeking, G. R., Chakrabarty, R. K. and Baumgardner, D.: Characterizing elemental, equivalent black, and refractory black carbon aerosol particles: a review of techniques, their limitations and uncertainties, Anal. Bioanal.Chem., 406(1), 99–122, doi:10.1007/s00216-013-7402-3, 2014.

Liati, A., Schreiber, D., Alpert, P. A., Liao, Y., Brem, B. T., Corral Arroyo, P., Hu, J., Jonsdottir, H. R., Ammann, M. and Dimopoulos Eggenschwiler, P.: Aircraft soot from conventional fuels and biofuels during ground idle and climb-out conditions: Electron microscopy and X-ray micro-spectroscopy, Environ. Pollut., 247, 658–667, doi:10.1016/j.envpol.2019.01.078, 2019.

Liu, F., Yon, J., Fuentes, A., Lobo, P., Smallwood, G. J. and Corbin, J. C.: Review of recent literature on the light absorption properties of black carbon: Refractive index, mass absorption cross section, and absorption function, Aerosol Sci. Technol., 54(1), 33–51, doi:10.1080/02786826.2019.1676878, 2020.

Lobo, P., Hagen, D. E. and Whitefield, P. D.: Comparison of PM emissions from a commercial jet engine burning conventional, biomass, and fischer-tropsch fuels, Environ. Sci. Technol., 45(24), doi:10.1021/es201902e, 2011.

Lobo, P., Christie, S., Khandelwal, B., Blakey, S. G. and Raper, D. W.: Evaluation of Non-volatile Particulate Matter Emission Characteristics of an Aircraft Auxiliary Power Unit with Varying Alternative Jet Fuel Blend Ratios, Energy Fuels, 29(11), 7705–7711, doi:10.1021/acs.energyfuels.5b01758, 2015a.

Lobo, P., Durdina, L., Smallwood, G. J., Rindlisbacher, T., Siegerist, F., Black, E. A., Yu, Z., Mensah, A. A., Hagen, D. E., Miake-Lye, R. C., Thomson, K. A., Brem, B. T., Corbin, J. C., Abegglen, M., Sierau, B., Whitefield, P. D. and Wang, J.: Measurement of aircraft engine non-volatile PM emissions: Results of the Aviation-Particle Regulatory Instrumentation Demonstration Experiment (A-PRIDE) 4 campaign, Aerosol Sci. Technol., 49(7), 472–484, doi:10.1080/02786826.2015.1047012, 2015b.

Lobo, P., Hagen, D. E., Whitefield, P. D. and Raper, D.: PM emissions measurements of in-service commercial aircraft engines during the Delta-Atlanta Hartsfield Study, Atmos. Environ., 104, 237–245, doi:10.1016/j.atmosenv.2015.01.020, 2015c.

Lobo, P., Condevaux, J., Yu, Z., Kuhlmann, J., Hagen, D. E., Miake-Lye, R. C., Whitefield, P. D. and Raper, D. W.: Demonstration of a Regulatory Method for Aircraft Engine Nonvolatile PM Emissions Measurements with Conventional and Isoparaffinic Kerosene fuels, Energy Fuels, 30(9), 7770–7777, doi:10.1021/acs.energyfuels.6b01581, 2016.

Lobo, P., Durdina, L., Brem, B. T., Crayford, A. P., Johnson, M. P., Smallwood, G. J., Siegerist, F., Williams, P. I., Black, E. A., Llamedo, A., Thomson, K. A., Trueblood, M. B., Yu, Z., Hagen, D. E., Whitefield, P. D., Miake-Lye, R. C. and Rindlisbacher, T.: Comparison of standardized sampling and measurement reference systems for aircraft engine non-volatile particulate

matter emissions, J. Aerosol Sci., 145, 105557, doi:10.1016/j.jaerosci.2020.105557, 2020.

Masiol, M. and Harrison, R. M.: Aircraft engine exhaust emissions and other airport-related contributions to ambient air pollution: A review, Atmos. Environ., 95, 409–455, doi:10.1016/j.atmosenv.2014.05.070, 2014.

Michelsen, H. A., Schulz, C., Smallwood, G. J. and Will, S.: Laser-induced incandescence: Particulate diagnostics for combustion, atmospheric, and industrial applications, Prog. Energy Combust. Sci., 51, 2–48, doi:10.1016/j.pecs.2015.07.001, 2015.

Modini, R. L., Corbin, J. C., Brem, B. T., Irwin, M., Bertò, M., Pileci, R. E., Fetfatzis, P., Eleftheriadis, K., Henzing, B., Moerman, M. M., Liu, F., Müller, T. and Gysel-Beer, M.: Detailed characterization of the CAPS single-scattering albedo monitor (CAPS PMssa) as a field-deployable instrument for measuring aerosol light absorption with the extinction-minus-scattering method, Atmos. Meas. Tech., 14(2), doi:10.5194/amt-14-819-2021, 2021.

Momenimovahed, A. and Olfert, J. S.: Effective Density and Volatility of Particles Emitted from Gasoline Direct Injection Vehicles and Implications for Particle Mass Measurement, Aerosol Sci. Technol., 49(11), 1051–1062, doi:10.1080/02786826.2015.1094181, 2015.

Moore, R. H., Thornhill, K. L., Weinzierl, B., Sauer, D., D'Ascoli, E., Kim, J., Lichtenstern, M., Scheibe, M., Beaton, B., Beyersdorf, A. J., Barrick, J., Bulzan, D., Corr, C. A., Crosbie, E., Jurkat, T., Martin, R., Riddick, D., Shook, M., Slover, G., Voigt, C., White, R., Winstead, E., Yasky, R., Ziemba, L. D., Brown, A., Schlager, H. and Anderson, B. E.: Biofuel blending reduces particle emissions from aircraft engines at cruise conditions, Nature, 543(7645), 411–415, doi:10.1038/nature21420, 2017.

Nakayama, T., Kondo, Y., Moteki, N., Sahu, L. K., Kinase, T., Kita, K. and Matsumi, Y.: Size-dependent correction factors for absorption measurements using filter-based photometers: PSAP and COSMOS, J. Aerosol Sci., 41(4), 333–343, doi:10.1016/j.jaerosci.2010.01.004, 2010.

Nakayama, T., Suzuki, H., Kagamitani, S., Ikeda, Y., Uchiyama, A. and Matsumi, Y.: Characterization of a Three Wavelength Photoacoustic Soot Spectrometer ({PASS}-3) and a Photoacoustic Extinctiometer ({PAX}), J. Meteorol. Soc. Japan. Ser. {II}, 93(2), 285–308, doi:10.2151/jmsj.2015-016, 2015.

Ogren, J. A., Wendell, J., Andrews, E. and Sheridan, P. J.: Continuous light absorption photometer for long-Term studies, Atmos. Meas. Tech., 10(12), 4805–4818, doi:10.5194/amt-10-4805-2017, 2017.

Onasch, T. B., Massoli, P., Kebabian, P. L., Hills, F. B., Bacon, F. W. and Freedman, A.: Single Scattering Albedo Monitor for Airborne Particulates, Aerosol Sci. Technol., 49(4), 267–279, doi:10.1080/02786826.2015.1022248, 2015.

Perim De Faria, J., Bundke, U., Freedman, A., Onasch, T. B. and Petzold, A.: Laboratory validation of a compact single-scattering albedo (SSA) monitor, Atmos. Meas. Tech., 14(2), 1635–1653, doi:10.5194/amt-14-1635-2021, 2021.

Petzold, A., Ogren, J. A., Fiebig, M., Laj, P., Li, S.-M., Baltensperger, U., Holzer-Popp, T., Kinne, S., Pappalardo, G., Sugimoto, N., Wehrli, C., Wiedensohler, A. and Zhang, X.-Y.: Recommendations for the interpretation of "black carbon" measurements, Atmos. Chem. Phys., 13(16), 8365–8379, doi:10.5194/acp-13-8365-2013, 2013.

SAE International. Aerospace Information Report (AIR) 6241 . Procedure for the Continuous Sampling and Measurement of Non-Volatile Particle Emissions from Aircraft Turbine Engines. Warrendale, PA, 2013. https://doi.org/10.4271/AIR6241

SAE international. Aerospace Recommended Practice (ARP) 6320 - Procedure for the Continuous Sampling and Measurement of Non-Volatile Particulate Matter Emissions from Aircraft Turbine Engines, Warrendale, PA, 2018. https://doi.org/10.4271/ARP6320.

SAE International. Aerospace Information Report (AIR) 6504 - Procedure for the Calculation of Sampling System Penetration Functions and System Loss Correction Factors, Warrendale, PA, 2017. https://doi.org/10.4271/AIR6504

SAE International. Aerospace Recommended Practice (ARP) 6481- Procedure for the Calculation of Sampling Line Penetration Functions and Line Loss Correction Factors, Warrendale, PA, 2019. https://doi.org/10.4271/ARP6481

Saffaripour, M., Thomson, K. A., Smallwood, G. J. and Lobo, P.: A review on the morphological properties of non-volatile particulate matter emissions from aircraft turbine engines, J. Aerosol Sci., 139, doi:10.1016/j.jaerosci.2019.105467, 2020.

Schindler, W., Haisch, C., Beck, H. A., Niessner, R., Jacob, E. and Rothe, D.: A photoacoustic sensor system for time resolved quantification of diesel soot emissions, SAE Technical Paper 2004-01-0968, SAE International., doi:10.4271/2004-01-0968, 2004.

Schripp, T., Anderson, B. E., Bauder, U., Rauch, B., Corbin, J. C., Smallwood, G. J., Lobo, P., Crosbie, E., Shook, M. E., Miake-Lye, R., Yu, Z., Freedman, A., Whitefield, P. D., Robinson, C. E., Achterberg, S. L., Köhler, M., Oßwald, P., Grein, T., Sauer, D., Voigt, C., Schlager, H., LeClercq, P. Aircraft engine particulate matter and gaseous emissions from sustainable aviation fuels: results from ground-based measurements during the NASA/DLR Campaign ECLIF2/ND-MAX. Submitted to Fuel. 2022.

Schripp, T., Anderson, B., Crosbie, E. C., Moore, R. H., Herrmann, F., Oßwald, P., Wahl, C., Kapernaum, M., Köhler, M., Le Clercq, P., Rauch, B., Eichler, P., Mikoviny, T. and Wisthaler, A.: Impact of Alternative Jet Fuels on Engine Exhaust Composition during the 2015 ECLIF Ground-Based Measurements Campaign, Environ. Sci. Technol., 52(8), 4969–4978, doi:10.1021/acs.est.7b06244, 2018.

Schripp, T., Herrmann, F., Oßwald, P., Köhler, M., Zschocke, A., Weigelt, D., Mroch, M. and Werner-Spatz, C.: Particle emissions of two unblended alternative jet fuels in a full scale jet engine, Fuel, 256, 115903, doi:10.1016/j.fuel.2019.115903, 2019.

Snelling, D. R., Smallwood, G. J., Liu, F., Gülder, Ö. L. and Bachalo, W. D.: A calibration-independent laser-induced incandescence technique for soot measurement by detecting absolute light intensity, Appl. Opt., 44(31), 6773, doi:10.1364/ao.44.006773, 2005.

Timko, M. T., Yu, Z., Onasch, T. B., Wong, H. W., Miake-Lye, R. C., Beyersdorf, A. J., Anderson, B. E., Thornhill, K. L., Winstead, E. L., Corporan, E., Dewitt, M. J., Klingshirn, C. D., Wey, C., Tacina, K., Liscinsky, D. S., Howard, R. and Bhargava, A.: Particulate emissions of gas turbine engine combustion of a fischer-tropsch synthetic fuel, Energy Fuels, 24(11), 5883–5896, doi:10.1021/ef100727t, 2010.

Timko, M. T., Fortner, E., Franklin, J., Yu, Z., Wong, H. W., Onasch, T. B., Miake-Lye, R. C. and Herndon, S. C.: Atmospheric measurements of the physical evolution of aircraft exhaust plumes, Environ. Sci. Technol., 47(7), 3513–3520, doi:10.1021/es304349c, 2013.

Trueblood, M. B., Lobo, P., Hagen, D. E., Achterberg, S. C., Liu, W. and Whitefield, P. D.: Application of a hygroscopicity tandem differential mobility analyzer for characterizing PM emissions in exhaust plumes from an aircraft engine burning conventional and alternative fuels, Atmos. Chem. Phys., 18(23), doi:10.5194/acp-18-17029-2018, 2018.

Ugarte, D.: Curling and closure of graphitic networks under electron-beam irradiation, Nature, 359(6397), 707–709, doi:10.1038/359707a0, 1992.

Virkkula, A.: Erratum: Calibration of the 3-wavelength particle soot absorption

1183 photometer (3λ PSAP) (Aerosol Science and Technology (2002) 39 (68-83)), Aerosol Sci.
1184 Technol., 44(8), 706–712, doi:10.1080/02786826.2010.482110, 2010.

1185 Vozka, P., Vrtiška, D., Šimáček, P. and Kilaz, G.: Impact of Alternative Fuel Blending
1186 Components on Fuel Composition and Properties in Blends with Jet A, Energy Fuels, 33(4),
1187 3275–3289, doi:10.1021/acs.energyfuels.9b00105, 2019.

1188 Vander Wal, R. L. and Choi, M. Y.: Pulsed laser heating of soot: morphological changes,
1189 Carbon N. Y., 37(2), 231–239, doi:10.1016/S0008-6223(98)00169-9, 1999.

1190 Vander Wal, R. L., Bryg, V. M. and Huang, C.-H.: Aircraft engine particulate matter: Macro-
1191 micro- and nanostructure by HRTEM and chemistry by XPS, Combust. Flame, 161(2), 602–
1192 611, doi:10.1016/j.combustflame.2013.09.003, 2014.

1193 Williams, P. I., Allan, J. D., Lobo, P., Coe, H., Christie, S., Wilson, C., Hagen, D., Whitefield, P.,
1194 Raper, D. and Rye, L.: Impact of alternative fuels on emissions characteristics of a gas
1195 turbine engine - Part 2: Volatile and semivolatile particulate matter emissions, Environ.
1196 Sci. Technol., 46(19), doi:10.1021/es301899s, 2012.

1197 Wilson, G. R., Edwards, T., Corporan, E. and Freerks, R. L.: Certification of alternative
1198 aviation fuels and blend components, Energy Fuels, 27(2), 962–966,
1199 doi:10.1021/ef301888b, 2013.

1200 Yuan, R., Lobo, P., Smallwood, G. J., Johnson, M. P., Parker, M. C., Butcher, D., &
1201 Spencer, A. (2022). Measurement of black carbon emissions from multiple engine
1202 and source types using laser-induced incandescence: sensitivity to laser fluence.
1203 Atmospheric Measurement Techniques, 15(2), 241–259. doi:10.5194/amt-15-241-
1204 2022. 2022.

1205

Formatted: Font: Not Italic

Formatted: Font: Not Italic

1206 ## 7 Figures and Tables

1207 Table 1. Properties of the fuels used for the ground-based measurements (fuel
1208 samples acquired from wing-tank after test).

Property	Method	JP-8	REF3	REF4	SAF1	SAF2	SAF3
Aromatics [vol%]	ASTM D1319	19.9	18.6	16.5	8.5	9.5	15.2
Hydrogen H [mass%]	ASTM D7171	13.86	13.65	14.08	14.40	14.51	14.04
Sulphur, total [ppm]	ISO 20884	1240	105	5.7	56.8	4.1	58.6
Naphthalenes [mass%]	ASTM D1840	1.49	1.17	0.13	0.61	0.05	0.64
Smoke point [mm]	ASTM D1322	23.0	23.0	27.0	30.0	30.0	28.0

Deleted: 9.6

Deleted: 10.8

1209

1212 Table 2. Instruments used to measure nvPM and key measured properties. All instruments reported data at 1 second intervals except the
1213 SMPSs (45 second intervals for NRC and DLR, 60 seconds for NASA) and filter samplers. Instrument abbreviations are defined in the text.

Operator	Instrument	Acronym	Species measured	Sampling duration [s]	Units	Penetration functions[d]
NASA	Particle soot absorption photometer	PSAP	nvPM[a] mass	1	$\mu g\ m^{-3}$	1
	Tricolor absorption photometer	TAP	nvPM[a] mass	1	$\mu g\ m^{-3}$	1
	Scanning mobility particle sizer	SMPS	Total PSD (10 to 278 nm)	45	particles cm^{-3}, and $\mu g\ m^{-3}$	1
	Thermo-denuder with SMPS	TD-SMPS	nvPM PSD[b] (10 to 278 nm)	45	$\mu g\ m^{-3}$	1, 4
	CO_2 sensor	LI-COR 7000	CO_2	1	ppmv	-
NRC	Cavity-attenuated phase shift PM_{SSA} monitor (660 nm)	CAPS (NRC)	nvPM[a] mass	1	$\mu g\ m^{-3}$	1
	Photoacoustic extinctiometer	PAX	nvPM[a] mass	1	$\mu g\ m^{-3}$	1
	Laser-induced-incandescence	LII 300 (NRC; 2x)	nvPM[b] mass	1	$\mu g\ m^{-3}$	1
	Catalytic stripper SMPS	CS-SMPS	nvPM PSD (8.6 to 278 nm)	45	particles cm^{-3}	1, 3
MST (NARS)	AVL Particle Counter Advanced	APC	nvPM number	1	particles cm^{-3}	1, 2
	Micro Soot Sensor	MSS Plus	nvPM[a] mass	1	$\mu g\ m^{-3}$	1, 2
	Laser-induced-incandescence	LII-300 (NARS)	nvPM[c] mass	1	$\mu g\ m^{-3}$	1, 2
	CO_2 sensor	LI-COR 840A	CO_2	1	ppm	-
	Differential mobility spectrometer	DMS500	Total PSD (5 to 1000 nm)	1	particles cm^{-3}	1, 2
ARI	Cavity-attenuated phase shift PM_{SSA} monitor (630 nm)	CAPS (ARI)	nvPM[a] mass	1	$\mu g\ m^{-3}$	1, 2

1214 [a]nvPM measured via particulate absorption as equivalent BC (eBC). [b]Particle size distribution, here measured with respect to mobility diameter. [c]nvPM measured
1215 via laser-induced incandescence as refractory BC (rBC). [d]Numbers are indices corresponding to the penetration functions shown in Figure 4.

1216 Table 3. Summary of the ratios between the EI_m of individual instruments and the
1217 geometric mean of the Group 1 (real time) instruments. The corresponding raw
1218 data are shown in Figure 11. Regression: linear regression against Group 1
1219 geometric mean weighted by standard deviations, with k = 2 uncertainties from fit.
1220 SD: standard deviation. RSD: Relative SD. Group 1: real time instruments. Group 2:
1221 integrative instruments.

1222

		EI_{mass} Ratio vs. Group 1			Regression vs. Group 1	
Group	Instrument	Mean	SD	RSD [%]	Intercept	Slope
1	CAPS PM$_{SSA}$ (ARI)	0.84	0.08	10	12 ± 19	0.8 ± 0.1
1	CAPS PM$_{SSA}$ (NRC)	0.99	0.09	9	-0.3 ± 0.8	1.01 ± 0.04
1	LII (NARS)	1.24	0.18	15	27 ± 6	1.03 ± 0.04
1	LII (NRC-0331)	1.07	0.1	9	-15 ± 42	1.17 ± 0.16
1	LII (NRC-0574)	0.78	0.08	10	-17.1 ± 2	0.88 ± 0.08
1	MSS+	1.07	0.14	13	17.8 ± 5	0.92 ± 0.04
1	PAX	1.06	0.18	17	-15 ± 1	1.21 ± 0.02
2	CS-SMPS	1.50	0.27	18	12 ± 22	1.02 ± 0.12
2	TD-SMPS	1.14	0.26	23	-5 ± 1	1.47 ± 0.04
2	PSAP	0.89	0.32	36	8 ± 16	0.82 ± 0.08
2	TAP	0.88	0.12	14	6 ± 6	0.75 ± 0.02

Formatted: Centered

1223

1224
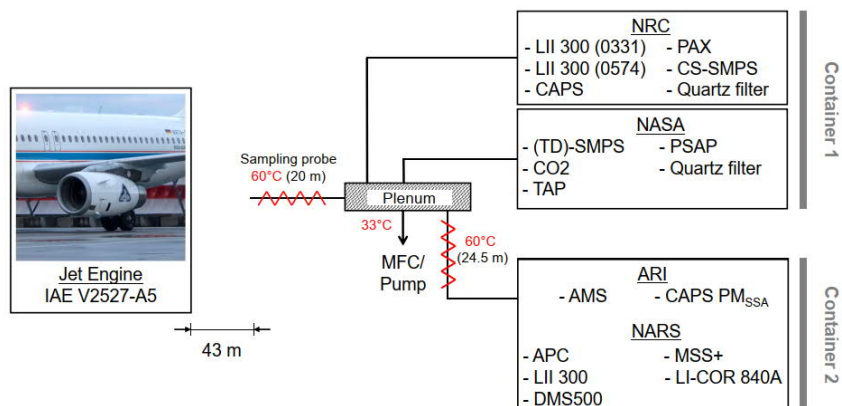
1225 Figure 1. Schematic of sampling configuration behind the DLR ATRA aircraft. The length
1226 and flow rate of sampling lines from the manifold to the various instruments varied as
1227 described in the text. The NRC and NASA instruments were all placed within Container 1,
1228 while the NARS and ARI instruments were placed in Container 2. For simplicity, the figure
1229 omits a short heated line connecting the first plenum to the NARS. The ARI instruments
1230 were downstream of all NARS instruments except the DMS500 (see Lobo et al., 2016 for
1231 detailed NARS diagram). NARS = North American Reference System.

1232
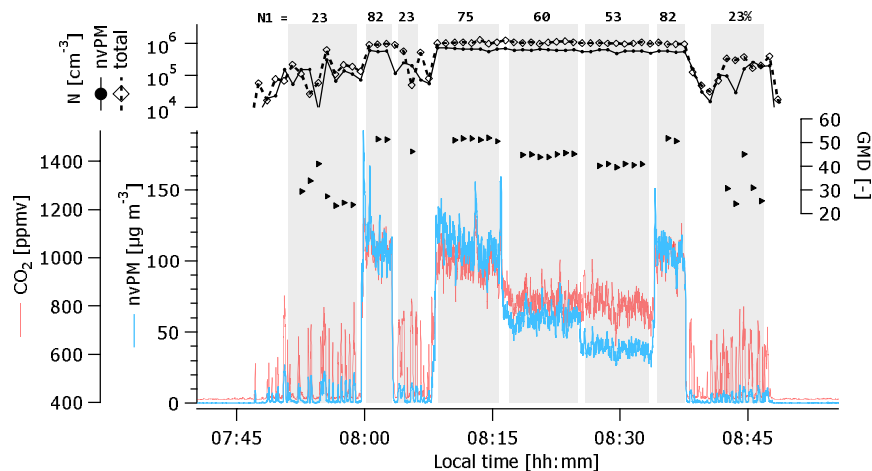
1233 Figure 2. Illustration of a typical test run. Variation in the CO_2 concentration was not due
1234 to instrument noise, as illustrated by the CO_2 measurements prior to and following
1235 sampling. A representative nvPM mass instrument is shown by the blue trace. Sizing
1236 information (GMD) is shown by the black symbols (triangles: GMD; diamonds with dashed
1237 line: total PM number; spheres with solid line: nvPM number measured with the CS-
1238 SMPS).

1239

1240
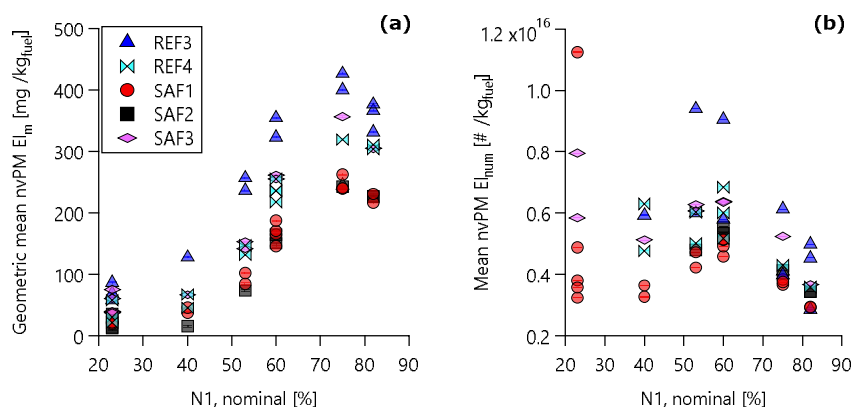
Figure 3. Relationship between nvPM (a) EI_m and (b) EI_{num} with N1 for all data obtained with the V2527-A5 engine. The trends shown in this plot are discussed further in the companion article (Schripp et al., 2022). The ordinate values are the geometric mean discussed in the text.

1241
1242
1243
1244

1245

1246
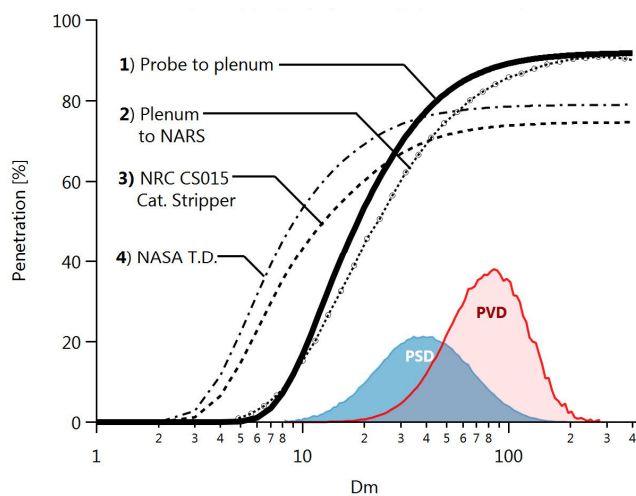
Figure 4. Penetration functions for the main probe-to-plenum sampling line as well as other components in the sampling system. Shaded areas illustrate a representative particle size (PSD) and volume (PVD) distribution measurement with GMD 34 nm and GSD 1.72. PSD data for all test points and instruments are provided in the supplement. NARS: North American Reference System; CS015: Catalytic Stripper; T.D.: thermodenuder.

1247
1248
1249
1250
1251
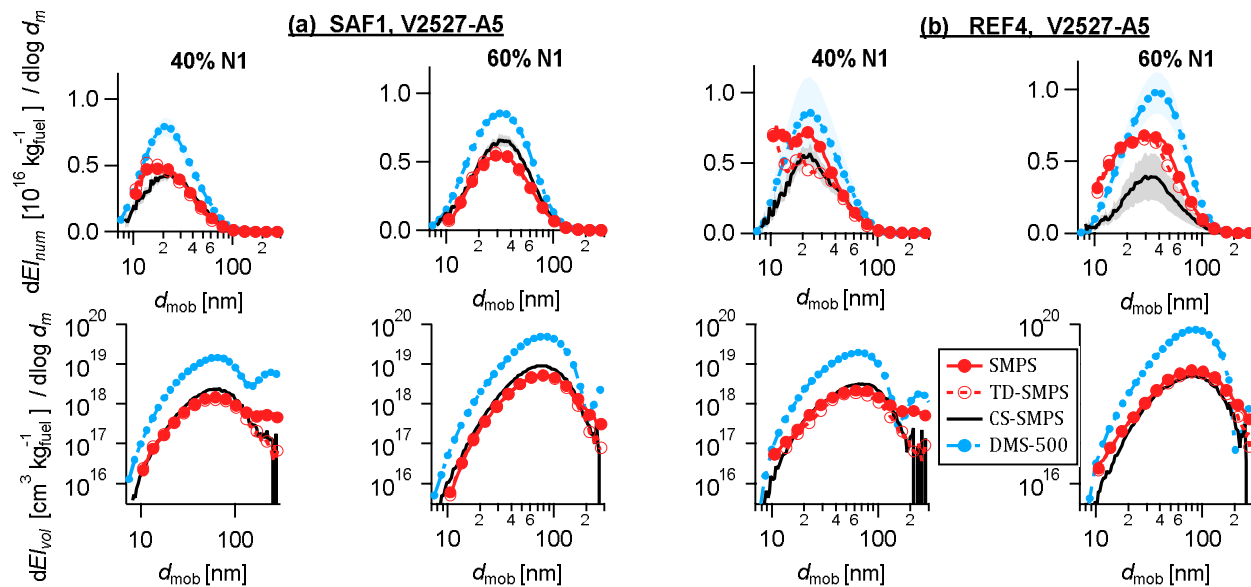
1257 Figure 5. Selected PSDs illustrating the V2527-A5 engine with (a) SAF1 fuel and (b) REF4 fuel. Each panel shows 60% N1 on the right and a lower N1
1258 on the left: 40% for (a), 60% for (b). Note that the TD-SMPS and CS-SMPS (red open circles and black line) represent nvPM, while the SMPS and
1259 DMS500 represent vPM.
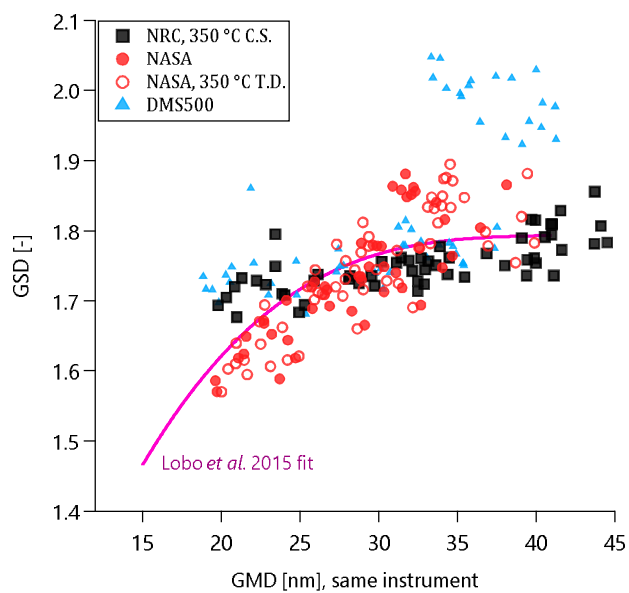
Figure 6. GSD versus GMD data as by measured by each particle sizer for all test points. Higher GSDs for the DMS500 correspond to bimodal PSDs (non-volatile and volatile modes). Note that size-dependent particle losses (see penetration functions in Figure 4) may affect both GSD and GMD. Based on Figure 12, the TD-SMPS (NASA) data may be more accurate than the CS-SMPS data (see text). Fit is from Lobo et al. (2015c).

1266
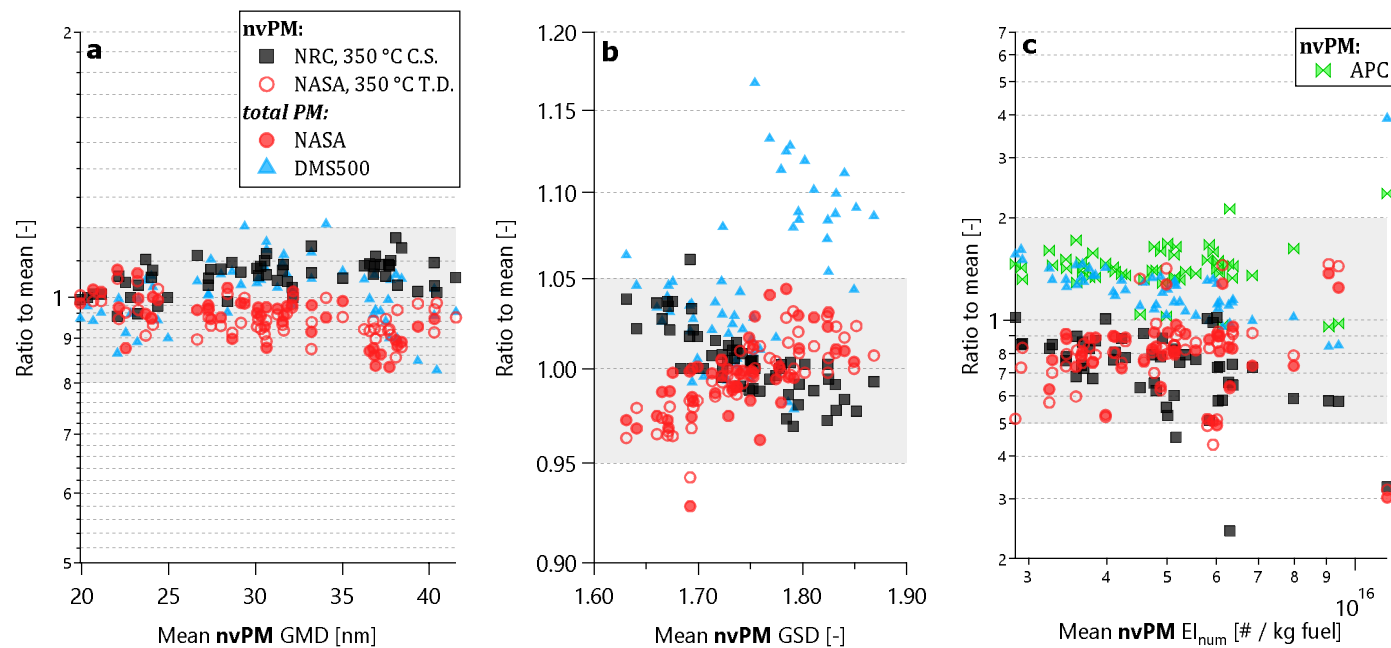
Figure 7. Comparison of size and number measurements in terms of GMD, GSD, and EI_n. Grey shading shows 20%, 5%, and 200% in GMD, GSD, and EI_n, respectively. In panels (a) and (b), mean is defined from the CS-SMPS (NRC) and TD-SMPS (NASA) data. In panel (c), the mean additionally includes the APC (NARS) data (the APC is in the NARS and uses a TSI 3790E CPC).

1270

1271
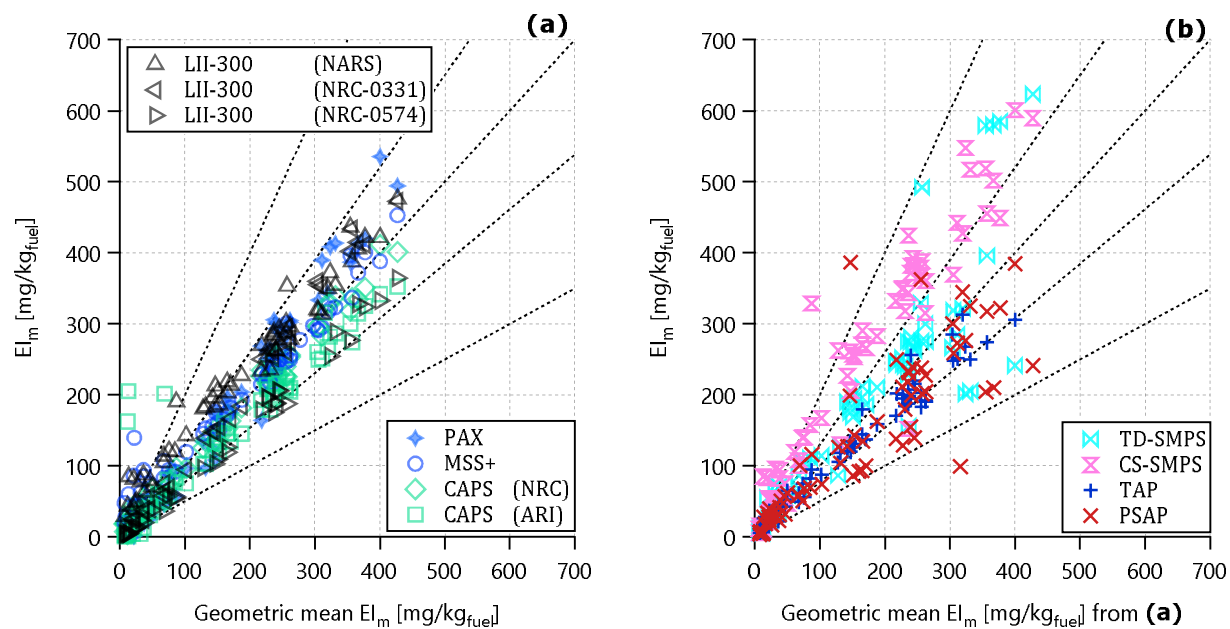
1272 Figure 8. EI_m scatterplot for (a) real-time and (b) integrative nvPM measurements. The term integrative refers to SMPS measurements (mass
1273 concentrations estimated by assuming unit-density spheres) and filter photometer measurements (mass concentrations estimated using standard
1274 empirical relationships between light attenuation and light absorption). The abscissa of both panels is the geometric mean of all available data from
1275 the 7 real-time sampling instruments plotted in (a). Angled lines illustrate slopes of 2, 2^{-1}, 1.3, 1.3^{-1}, and 1.0.
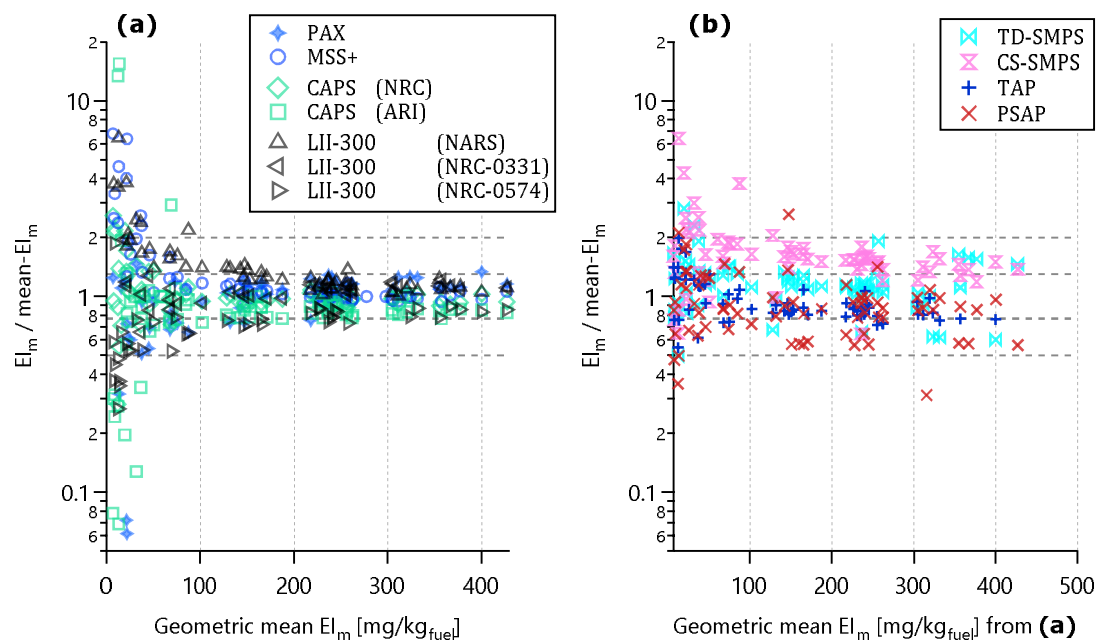
Figure 9. Ratio plots corresponding to Figure 8. The inner and outer horizontal lines show ratios of 2, 2^{-1}, 1.3, 1.3^{-1}, and 1.0. Agreement between the instruments is poorer at $EI_m < 100$ mg/kg$_{fuel}$, which corresponds to an approximate concentration of 10 µg m^{-3} (the exact conversion factor varies with CO_2 concentration and fuel properties) and close to the limit of detection for most instruments.
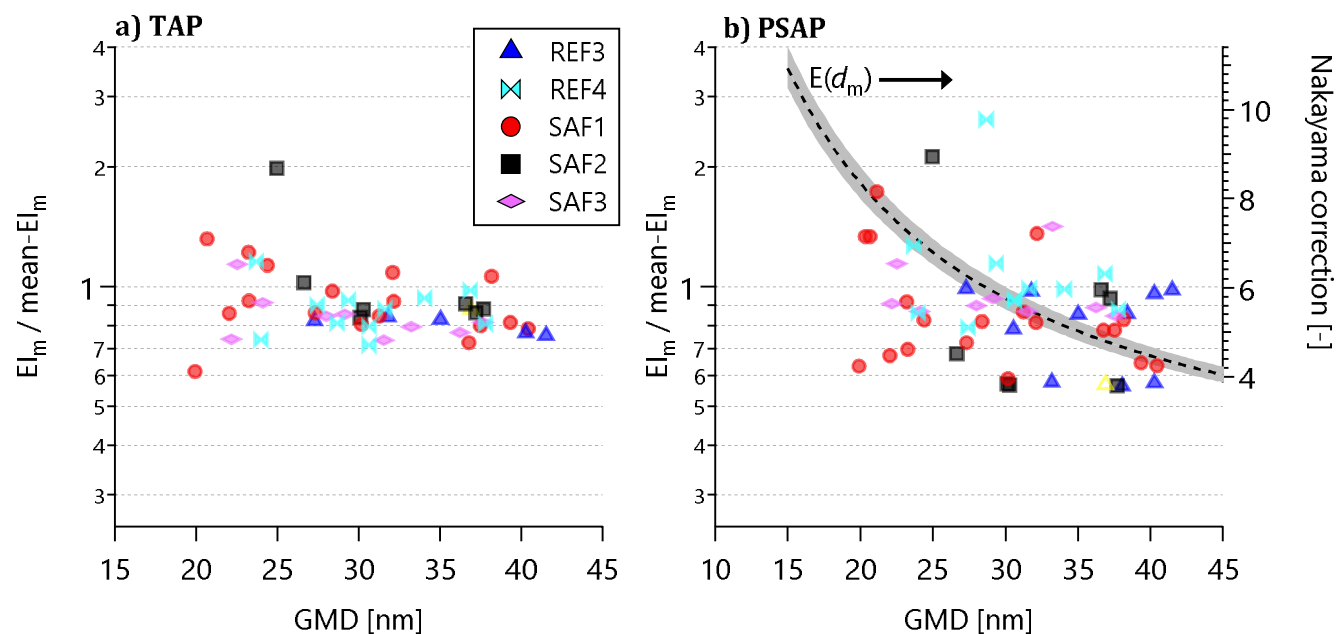
1281 Figure 10. EI_m/ mean-EI_m ratios from Figure 9 for the TAP and PSAP (the filter-based photometers) only, plotted as a function of geometric mean
1282 mobility diameter (GMD) to highlight potential size-dependent sensitivities of these instruments. The curve labelled $E(d_m)$ in b) plots the size-
1283 dependent PSAP correction factor given by Nakayama et al. (2010; Eq. 8) with 1σ uncertainties shaded.
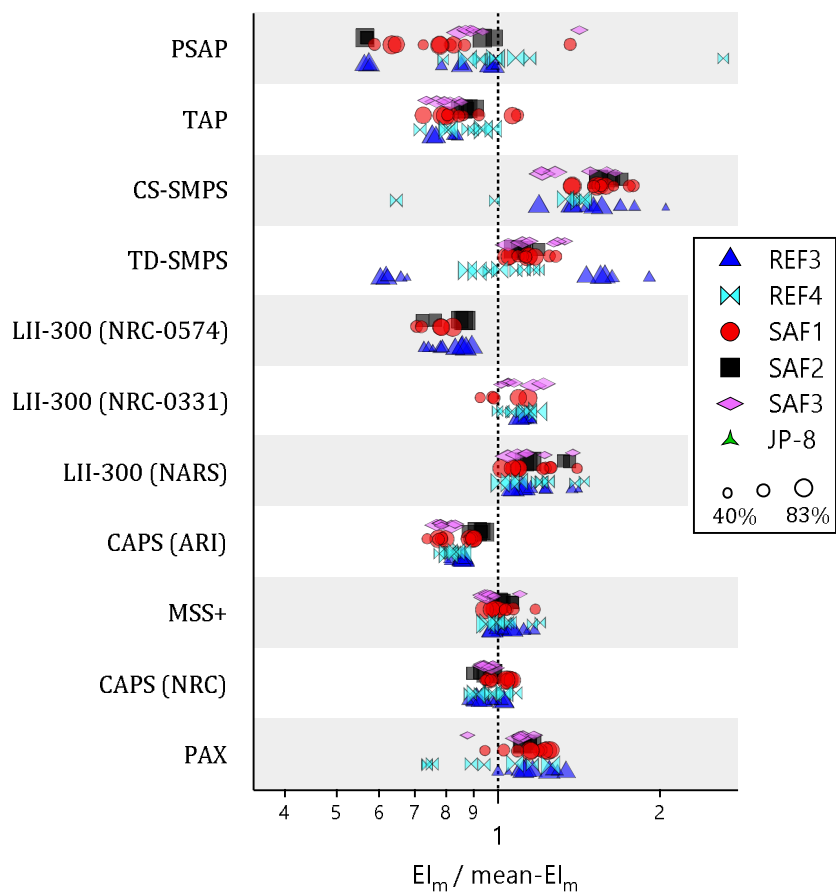
Figure 11. Ratios of Figure 9 grouped by fuel. All fuels except JP-8 were combusted in the V2527-A5 engine; JP-8 was combusted in the CFM56-2C1 engine. Shading is to guide the eye. Symbols are sized by N1 thrust. Plot excludes data where $EI_m < 25$ mg/kg$_{fuel}$ and N1 thrust below 40% to minimize the effects of instrument noise and wind speed, respectively, on the ratios.
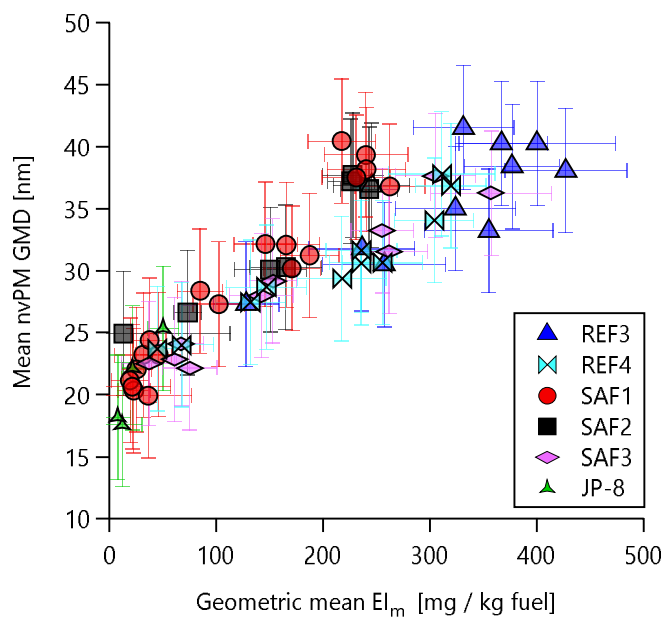
Figure 12. Scatterplot of the mean nvPM GMD within test points against geometric
mean nvPM EI_m from Figure 8a. The correlation with GMD and EI_m indicates that Figure 9
implicitly represented different particle sizes.
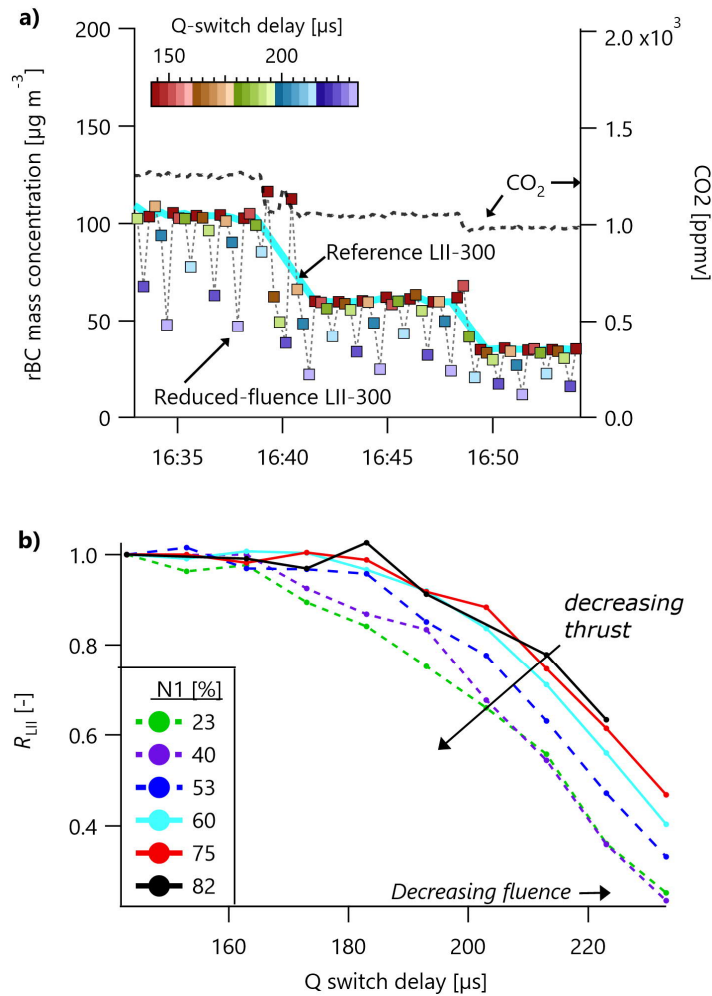
1297   Figure 13. (a) LII 300 experiment time series, where one LII 300 was operated with

1298   increased Q-switch delays to reduce its laser fluence (squares) and the other was operated

1299   at standard fluence (solid line). CO_2 data are also shown for context. (b) The ratio R_{LII} of

1300   the concentration reported by the reduced-fluence LII divided by the reference LII. It is

1301   evident from (b) that the standard high-fluence conditions generate data that are

1302   independent of N1 thrust, and that moderate- and low-fluence conditions (Q-switch delays

1303   greater than about 165 to 185 µs) display a weak dependence on thrust.

1304